

REPORT DOCUMENTATION PAGE				Form Approved OMB No. 0704-0188	
1a. REPORT SECURITY CLASSIFICATION Unclassified			1b. RESTRICTIVE MARKINGS		
AD-A219 624			3. DISTRIBUTION/AVAILABILITY OF REPORT Approved for public release; distribution is unlimited.		
6a. NAME OF PERFORMING ORGANIZATION Massachusetts Institute of Technology			5. MONITORING ORGANIZATION REPORT NUMBER(S) AFOSR-TR-90-0283		
6b. ADDRESS (City, State, and ZIP Code) 77 Massachusetts Avenue Cambridge, MA 02139			7a. NAME OF MONITORING ORGANIZATION AFOSR/NA		
8a. NAME OF FUNDING/SPONSORING ORGANIZATION AFOSR/NA			7b. ADDRESS (City, State, and ZIP Code) Building 410, Bolling AFB DC 20332-6448		
8b. OFFICE SYMBOL (if applicable) NA			9. PROCUREMENT INSTRUMENT IDENTIFICATION NUMBER AFOSR 84-0356		
8c. ADDRESS (City, State, and ZIP Code) Building 410, Bolling AFB DC 20332-6448			10. SOURCE OF FUNDING NUMBERS		
			PROGRAM ELEMENT NO. 61102F	PROJECT NO. 2308	TASK NO. A2
11. TITLE (Include Security Classification) (U) Numerical Simulation of Turbulent Combustion Using Vortex Methods					
12. PERSONAL AUTHOR(S) Ahmed F. Ghoniem					
13a. TYPE OF REPORT Final Technical		13b. TIME COVERED FROM 1986 TO 1989		14. DATE OF REPORT (Year, Month, Day) 1990 January 8	
15. PAGE COUNT 79					
16. SUPPLEMENTARY NOTATION					
17. COSATI CODES			18. SUBJECT TERMS (Continue on reverse if necessary and identify by block number)		
FIELD	GROUP	SUB-GROUP	Reynolds Number, Navier-Stokes Equations, Turbulent Combustion, Vortex Methods, Fluid Mechanics Numerical Simulation, Lagrangian Functions		
19. ABSTRACT (Continue on reverse if necessary and identify by block number) During the course of this work, we have developed a new numerical method for the integration of the unaveraged, time-dependent, high-Reynolds number Navier-Stokes equations governing a reacting flow. This method, which we called the transport element, is a grid free Lagrangian field method which has been developed for the simulation of reacting flow, and to describe mechanisms of shear flow-combustion interaction which have been revealed using these methods.					
20. DISTRIBUTION/AVAILABILITY OF ABSTRACT <input checked="" type="checkbox"/> UNCLASSIFIED/DUNLIMITED <input type="checkbox"/> SAME AS RPT. <input checked="" type="checkbox"/> DTIC USERS			21. ABSTRACT SECURITY CLASSIFICATION Unclassified		
22a. NAME OF RESPONSIBLE INDIVIDUAL Julian M Tishkoff			22b. TELEPHONE (Include Area Code) (202)767-0465		22c. OFFICE SYMBOL AFOSR/NA

FINAL REPORT
ON
NUMERICAL SIMULATION OF TURBULENT COMBUSTION USING VORTEX METHODS

(AFOSR Grant No. 84-0356)

Principal Investigator:

Ahmed F. Ghoniem

Department of Mechanical Engineering
Massachusetts Institute of Technology
Cambridge, MA 02139

SUMMARY

During the course of this work, we have developed a new numerical method for the integration of the unaveraged, time-dependent, high-Reynolds number Navier-Stokes equations governing a reacting flow. This method, which we called the transport element, is a grid-free, Lagrangian field method which has been developed for the simulation of reacting flow, and to describe mechanisms of shear flow-combustion interaction which have been revealed using these methods.

Accession For	
NTIS GRA&I	<input checked="checked" type="checkbox"/>
DTIC TAB	<input type="checkbox"/>
Unannounced	<input type="checkbox"/>
Justification	
By	
Distribution/	
Availability Codes	
Dist	Avail and/or Special
A-1	



90 03 12 122

TABLE OF CONTENTS

PERSONNEL	2
PUBLICATIONS DURING 1988-1989	3
INTERACTIONS DURING 1988-1989	5
TECHNICAL REPORT 1984-1989	6
I. BACKGROUND	6
I.1. NUMERICAL ISSUES	6
I.2. CLASSIFICATION	7
I.3. ORGANIZATION	8
II. THE VORTEX ELEMENT METHOD IN 2D	11
II.1. NUMERICAL SCHEME	11
II.2. PRIMARY SHEAR FLOW INSTABILITY	13
III. THE VORTEX ELEMENT METHOD IN 3D	15
III.1. NUMERICAL SCHEME	16
III.2. VORTEX RINGS	17
III.3. SECONDARY INSTABILITIES IN SHEAR FLOWS	19
IV. THE TRANSPORT ELEMENT METHOD	22
IV.1. NUMERICAL SCHEME	23
IV.2. SCALAR MIXING IN SHEAR LAYERS	25
IV.3. ENTRAINMENT ENHANCEMENT DUE TO 3D	26
V. VORTEX METHOD FOR VARIABLE DENSITY	27
V.1. BAROCLINIC EFFECTS	28
VI. VORTEX METHODS FOR REACTING FLOW	30
VI.1. THE REACTING SHEAR LAYER	32
VI.2. 3D REACTING SHEAR LAYERS	34
VI.3. THE REACTING JET	36
VI.4. THE PREMIXED SHEAR LAYER	40
VII. EXTENSIONS	42
VIII. CLOSURE	43
REFERENCES	46
FIGURE CAPTIONS	50

PERSONNEL

Five graduate students completed their degrees during 1984-1989 under partial support of this program. Their names and theses title are:

1. Gagnon, Yves, Numerical Investigation of Recirculating Flow at Moderate Reynolds Numbers Using Vortex Methods, M.Sc. Thesis, February 1986.
2. Ng, K.K., Vortex Simulation of a Confined and Perturbed Mixing Layer, M.Sc. thesis, February 1986.
3. Heidarinejad, Ghassem, Numerical Simulation of a Reacting Shear Layer Using The Transport Element Method, Ph.D. thesis, February 1989.
4. Najm, Habib, Numerical Investigation of the Instability of Premixed Dump Combustors, Ph.D. thesis, June 1989.
5. Krishnan, Anantha, Numerical Study of Vorticity-Combustion Interactions in Shear Flow, Sc.D. thesis, August 1989.

Three graduate students are currently working on their theses under partial support from this contract. Their names and theses titles are:

1. Knio, Omar, Spanwise Structures in a Reacting Turbulent Mixing Layer: Solutions Using 3-D Vortex Methods, Ph.D. thesis, expected June 1990.
2. Loprenzo, T., Implementation of Reduced Chemical Kinetics Schemes in Vortex Simulation of Shear Flow, M.S. thesis, started September 1989.
3. Soteriou, Marios, Compressible Vortex Method for the simulation of high Mach Number Combustion, Ph.D. thesis, started September 1988.

PUBLICATIONS DURING 1988-1989:

1. Ghoniem, A.F., Heidarinejad, G. and Krishnan, A. "Numerical simulation of A Thermally-stratified Shear Layer Using the Vortex Element Method," J. Comput. Phys., 79, 1988, pp. 135-166. (*)
2. Krishnan, A. and Ghoniem, A.F. "Origin and Manifestation of Flow-Combustion Interaction in A Premixed Shear Layer," Proceedings of the 22nd Symposium (International) on Combustion, the Combustion Institute, Pittsburgh, PA, pp. 665-675. (*)
3. Knio, O.M. and Ghoniem, A.F. "Numerical Study of A Three-dimensional vortex method," J. Comput. Phys., in press, 1989.
4. Heidarinejad, G. and Ghoniem, A.F., "Vortex Simulation of the Reacting Shear Layer; Investigation of the Limits on the Rate of Burning," 27th AIAA Aerospace Sciences Meeting, Reno, Nevada, January 9-12, 1989, AIAA-89-0573. (*)
5. Ghoniem, A.F. and Krishnan, A, "Baroclinic Effects in Density-stratified Flows," submitted for publication, J. Fluid Mech, June 1989.
6. Ghoniem, A.F. and Krishnan, A. "Mixing Patterns and the Generation of Vorticity in Density Stratified Flow," presented at the International Workshop on The Physics of Compressible Turbulent Mixing, Princeton University, Princeton, N.J., October 24-27, 1988, in print.
7. Krishnan, A. and Ghoniem, A.F., "Numerical Simulation of the Structure of A Momentum/Gravity Driven Diffusion Flame," 27th AIAA Aerospace Sciences Meeting, Reno, Nevada, January 9-12, 1989, AIAA-89-0485. (*)
8. Ghoniem, A.F., Vortex Methods in Turbulent Reacting Flow, in Numerical Approaches to Combustion Modeling, ed by E. S. Oran and J. P. Boris, to be published by the AIAA, 1989.
9. Knio, O.M. and Ghoniem, A.F. "Three-dimensional Simulation of the Entrainment Augmentation Due to Streamwise Vortex Structures," 27th AIAA Aerospace Sciences Meeting, Reno, Nevada, January 9-12, 1989, AIAA-89-0574.
10. Knio, O.M., and Ghoniem, A.F., "Three Dimensional Vortex Simulation of Roll-up and Mixing in Shear Flow," submitted for publication at the Journal of Computational Physics, June 1989.
11. Krishnan, A. and Ghoniem, A.F., "Simulation of the rollup and mixing in Rayleigh-Taylor flow using the vortex/transport element method," submitted for publication at the Journal of Computational Physics, August 1989.
12. Ghoniem, A.F. and Krishnan, A. "Vorticity-combustion interactions in a turbulent reacting jet," presented at The 12th International Colloquium on Dynamics of Explosions and Reactive Systems, July 23-28, 1989, Ann Arbor, Michigan, Proceedings in print.
13. Najm, H. and Ghoniem, A.F., "Flame-Vorticity-Acoustic Interactions Leading to Combustor Instability," the AIAA/SAE/ASME/ASEE 25th Joint Propulsion Meeting, Monterey, CA, July 10-12, 1989. (*)

14. Ghoniem, A.F. and Heidarinejad, G., "The structure of the reaction zone in a reacting shear layer;" presented at The 12th International Colloquium on Dynamics of Explosions and Reactive Systems, July 23-28, 1989, Ann Arbor, Michigan, Proceedings in print.

15. Ghoniem, A.F., "Numerical Simulation of Turbulent Combustion using Vortex Methods," Invited five-lecture series at the University of Rome, Italy, June 24-28, 1989.

The P.I. delivered a number of invited seminars and presentations. A partial list is presented below:

1. Sandia Meeting on Turbulent Reacting Flow, General Electric Co., Schenectady, October 1988.
2. DOD and EPA Tyndall Conference on Halon, the Ozone Layer and Research on Alternative Chemicals, Tyndall, Florida, November 1988.
3. University of Connecticut, Storrs, November 1988.
4. University of California, Berkeley, April 1989.
5. Yale University, April 1989
6. Engineering Foundation Conference on Fluid Mechanics of Engine Combustion, Santa Barbara, May 1989
7. Gas Research Institute Meeting on Fluid Mechanics of Gas Burners, May 1989.
8. Berkeley Workshop on Vortex Methods, May 1989.

(*) Reprints are included with the report.

INTERACTIONS WITH INDUSTRIAL AND GOVERNMENT LABORATORIES DURING 1988-1989:

During the course of last year, we have started and/or continued collaborative working relations with the following industrial or governmental laboratories:

1. Wright-Patterson Laboratory; with Dr. M. Roquemore on the modeling of the jet diffusion flame.
2. General Electric Research Center; with Dr. Sanjay Corea on the study of turbulent premixed flames and their instability.
3. Sandia National Laboratory; with Drs. R. Lucht and John Kelly and their associates on the study of bluff-body diffusion flames.
4. Gas Research Institute; with Dr. J. Keizerle, on the numerical simulation of bluff body flame burners.
5. Ford Motor Company; with Mr. C. Kent and L. Ramai, on numerical simulation of flame propagation in enclosures and flow during intake processes.
6. Shell Oil Co.; with Dr. J.-C. Ginestra, on numerical simulation of flow, mixing and combustion in well-stirred reactors.
7. Allison Gas Turbine; with Dr. H. Mongia, on numerical simulation of streamwise vortex structures in thrust augmentor sections.
8. National Institute of Standards and Technology; with Dr. H. Baum, on numerical simulation of uncontrolled combustion.
9. Army Atmospheric Research Laboratory; with Mr. R. Meyers, numerical simulations of flow over complex terrains.

TECHNICAL REPORT

VORTEX SIMULATION OF REACTING SHEAR FLOW

I. BACKGROUND.

Consider the class of unsteady, high-Reynolds number, reacting-shear flows, including shear layers, jets, wakes and recirculating flows. These flows are characterized by a rapid growth of successive natural instabilities which lead to substantial changes in the geometry of the streamlines. The simulation of these flows, i.e., the solution of the unsteady, unaveraged governing equations, requires computational schemes which accommodate these geometrical changes, and in which numerical diffusion is maintained below physical diffusion without sacrificing numerical stability. One way to achieve this is to utilize schemes based on the Lagrangian formulation of the conservation equations.

In Lagrangian methods, grid points, where the flow variables are computed, are transported along particle trajectories. These methods offer natural ways to: (1) accommodate the severe distortion experienced by high-Reynolds number flows as they evolve through different states; (2) reduce the artificial diffusion encountered in numerical schemes in which spatial derivatives are discretized; and (3) account, in a balanced way, for physical diffusion in regions where the two modes of transport; convection and diffusion, are of the same order of magnitude. A brief discussion of these issues is presented.

I.1. NUMERICAL ISSUES

A challenge which is often encountered in numerical simulation of reacting shear flow is how to capture the severe distortion of the flow map which results from the nonlinear growth of natural flow instabilities. The saturation of these instabilities in the primary flow, which can normally be

characterized by almost parallel streamlines, results in a secondary flow with strongly curved streamlines. The latter often possesses secondary instabilities which evolve into tertiary flows. To accurately capture these changes using a numerical simulation, a very large number of fixed grid points, or a moving grid in which mesh points follow the distortion of the flow field is needed. The latter class belongs to Lagrangian schemes.

Convection is the dominant mechanism of transport at high Reynolds number. Convection in the cross-stream direction, perpendicular to the streamwise direction, is increased substantially by the growth of natural flow instabilities and their saturation into fully-developed flows. Meanwhile, diffusive transport cannot be ignored. Molecular diffusion is responsible for the transport of vorticity from solid walls into the interior in boundary layers, the mixing of species across material surfaces, and the transport of heat and species across laminar flames. Accurate simulation of diffusion is particularly crucial in reacting flows where mixing, most often, determines the burning rate. On the other hand, excessive numerical diffusion in an algorithm can artificially stabilize the flow. Numerical diffusion acts as a fictitious source of molecular diffusivity that reduces the effective Reynolds number of the computed flow. In combustion calculations, excessive mixing due to numerical diffusion tends to increase the burning rate. To capture the growth of flow instabilities while limiting diffusion to practically interesting values one needs to simulate flows at Reynolds number $O(10^3-10^5)$.

1.2. CLASSIFICATION

One class of Lagrangian methods, which has successfully been used in gas dynamics, utilizes grids to discretize flow derivatives., e.g., Lagrangian finite-difference methods. In this method, grid points are

transported along particle trajectories. Shear flow can lead to strong distortion of the grid and a concomitant loss of discretization accuracy. To maintain accuracy a long time after the action of strong shear, mesh regularization and remeshing become important [1-3].

On the other hand, grid-free, Lagrangian field methods, of the type described in this report, do not use approximations to spatial derivatives on a nonuniform mesh. Instead, computational elements are used to transport finite values of the spatial gradients of the variables, specifically vorticity and scalar gradients (scalars are temperature and species concentrations). Primitive variables, such as velocity and scalar concentrations, are obtained by integration over the strength of the transport elements. These methods are labelled field methods since each element induces a field of both its strength, e.g., the vorticity of an element extends over a finite area, and of the primitive variable it is transporting, e.g., the velocity induced by a vortex element extends to an infinitely large distance.

The goals of this report are to review Lagrangian field methods which have been developed for the simulation of compressible reacting flow, and to describe the mechanisms of shear flow-combustion interaction which have been revealed using these methods. These goals are achieved simultaneously by progressively introducing more complicated models, describing the necessary numerical algorithms and presenting their results in a form most relevant to the study of flow-combustion interaction. The models are gradually expanded until they include many of the physically interesting processes in combustion.

I.3. ORGANIZATION

Vortex methods, a particular class of grid-free Lagrangian field methods, have been used to obtain solutions of the momentum equation. These methods are based on the discretization of the vorticity among elements of finite area, and the transport of these elements along particle trajectories. The fact that vorticity is conserved along the particle trajectory in a two-dimensional, uniform-density flow makes these methods particularly simple. However, in Section II, we show that maintaining accuracy requires the application of elaborate vorticity-updating schemes as vortex elements are moved along particle trajectories when shear, or a strong strain field is present. The extension and application of vortex methods to three dimensional flows, where the conservation of vorticity along particle trajectories is not satisfied, also require the careful application of schemes to implement the effect of vortex stretch on the strength of the elements, as discussed in Section III. Solutions using the two and three-dimensional methods are discussed to illustrate some of the most common instabilities encountered in nonreacting and reacting shear flows and to reveal the mechanisms by which the maturation of these instabilities enhance mixing, and hence burning in a reacting flow.

The application of vortex methods to nonuniform density, reacting and compressible flows requires compatible Lagrangian, grid-free field schemes to compute the transport of scalars. For this purpose, we developed the transport element method to solve the convective-diffusive scalar transport equation. Even in a nonuniform density, incompressible flow, the transport of a scalar is required for the computations of the density field which affects the flow dynamically via the generation of baroclinic vorticity. The formulation of this method is described in Section IV, and the results of its application to compute scalar mixing in a shear layer are reviewed.

The transport element method is then combined with the vortex method to solve the problem of nonuniform density shear flow in Section V. Baroclinic vorticity generation is one of the important mechanisms by which combustion affects the fluid dynamics and, thus, the computational results on a nonuniform-density shear layer are reviewed in some detail in this section.

Another important mechanism of flow-combustion interaction, namely reaction extinction due to the formation of localized regions of strong strains as instabilities grow into their nonlinear range, is revealed by the results of incompressible reacting flow models. These results are discussed in section VI, after reviewing the formulation of the low-Mach number combustion model and the extension of the transport element method to accommodate the reaction terms in the conservation equations. Three-dimensional reacting shear layer simulations are presented to illustrate the complexity of the mixing pattern encountered in these flow and how they affect the structure of the burning zone. Compressible reacting flows exhibit another mechanism of combustion-flow interaction, namely the volumetric expansion associated with energy release within the reaction zone. Results of computations of combustion in heterogeneous and homogeneous compressible shear layers, using the transport element method, are reviewed to illustrate the origin and role of this mechanism.

The bulk of this report is devoted to a brief description of Lagrangian methods for the simulation of reacting flows in free shear layers, and a review of the most important mechanisms of flow-combustion interactions revealed by the application of these methods. Section VII briefly describes some extension of vortex methods to confined shear flow. We close the report with some thoughts on the needs for future development in the methodology and some areas of application which have not been explored.

II. THE VORTEX ELEMENT METHOD IN TWO DIMENSIONS.

The vorticity transport equation of a two-dimensional, incompressible, inviscid flow is:

$$\frac{\partial \omega}{\partial t} + \mathbf{u} \cdot \nabla \omega = 0, \quad (1)$$

where $\nabla \times \mathbf{u} = \omega$ and $\nabla \cdot \mathbf{u} = 0$. In the above, $\mathbf{u} = (u, v)$ is the velocity, ω is the vorticity, $\mathbf{x} = (x, y)$, t is time and $\nabla = (\partial/\partial x, \partial/\partial y)$. If $\chi(\mathbf{X}, t)$ describes a particle path, where \mathbf{X} is the Lagrangian coordinate of χ so that $\chi(\mathbf{X}, 0) = \mathbf{X}$, then Eq. (1) states that $\omega(\chi(\mathbf{X}, t), t) = \omega(\mathbf{X}, 0)$, i.e., vorticity is constant along particle trajectory. Thus, if the vorticity field at time $t = 0$ is divided among elements which move along particle trajectories, the strength, i.e., the vorticity of each element will remain the same. Moreover, it can be shown that $\mathbf{u}(\mathbf{x}, t) = \int \mathbf{K}(\mathbf{x} - \mathbf{x}') \omega(\mathbf{x}') d\mathbf{x}'$, $\mathbf{K}(\mathbf{x}) = -1/2\pi r^2 (-y, x)$ and $r^2 = x^2 + y^2$, which is the Biot-Savart law. This Lagrangian formulation of vorticity transport is the basis of vortex methods [4,5].

II.1. NUMERICAL SCHEME

In vortex methods, the vorticity field is discretized into a number of vortex elements of finite and overlapping cores:

$$\omega(\mathbf{x}, t) = \sum_{i=1}^N \omega_i h^2 f_\delta(\mathbf{x} - \chi_i(\mathbf{X}_i, t)), \quad (2)$$

where ω_i is the vorticity of an element, N is the total number of vortex elements, h is the average distance between the centers of neighboring elements in two principal directions, $h^2 = h_x h_y$, δ is the core radius of a vortex element, and $f_\delta = 1/\delta^2 f(r/\delta)$ is the core function describing the distribution of vorticity associated with an element.

The velocity field of a distribution of vortex elements is obtained by substituting Eq. (2) into the Biot-Savart law and performing the integration. The result is:

$$u(x, t) = \sum_{i=1}^N \omega_i h^2 K_\delta(x - X_i(X_i, t)), \quad (3)$$

where

$$\frac{dX_i}{dt} = u(X_i(X_i, t), t), \quad (4)$$

while $K_\delta(x) = K(x) \kappa(r/\delta)$ and $\kappa(r) = 2\pi \int_0^r f(r') r' dr'$.

Equation (2) is equivalent to expanding a function $\omega(x, t)$ in terms of a number, N , of kernel functions, f_δ , located at X_i and with weights $\omega_i h^2$. The accuracy of the discretization depends on the choice of f , the initial distribution of the particles, the evaluation of the values of ω_i , $i = 1, 2, \dots, N$, and the ratio of δ/h [6,7]. The selection of a core function to achieve given accuracy was extensively discussed in a number of theoretical analyses [8-11]. For the evaluation of the initial values of ω_i , we found that collocation on a uniform grid provides the best long time accuracy (collocation on a nonuniform grid may be a better choice when the initial vorticity field is highly nonuniform). We also found, using extensive numerical experimentation, that accurate discretization and long-time accuracy of the computed flow field require that $\delta = 1.1-1.5 h$. This choice of δ/h allows for strong overlap between the fields of the vortex elements. Thus, the local value of vorticity is determined by the contributions of many surrounding elements.

A strong strain, associated with the growth of perturbations into the nonlinear stages of the underlying instability, increases the distance between neighboring elements, δX , beyond the desired maximum value of h . Thus, the accuracy of the spatial discretization, which is governed by δ/h ,

is negatively affected and unorganized, random motion on the scale of h is encountered. This deterioration of accuracy is connected with the failure of vortex elements of fixed cores to accurately capture the distortion of the vorticity field locally. To circumvent this problem, more elements are introduced in areas where $\delta\chi > \beta h$, where $\beta \sim 1.5$. The circulation of the original elements is locally redistributed among the newly introduced elements, and the local value of vorticity is kept constant.

In the redistribution algorithm, conservation of vorticity is satisfied by dividing h^2 and δ^2 such that δ/h remains constant, i.e. the core radius of an element is decreased as the element is exposed to strong positive strain. An alternative way to capture the effect of strain on the geometry of the computational elements is to replace a circular elements by an elliptical element, while preserving its area, with its major axis aligned with the direction of maximum positive strain. If this was done, a circular vortex element would eventually become a vortex sheet with a velocity jump across its length equal to the local value of the vorticity ω_i . For computational convenience, however, we replace a strained circular element by several circular elements, aligned along the major axis of strain, but with smaller core radii than the original element [6].

II.2. PRIMARY SHEAR FLOW INSTABILITIES

We used shear layers as test cases for the validation of the numerical methods, and as generic problems for the study of flow-combustion interactions. We start with a two-dimensional, incompressible, nonreacting flow, and build up to three-dimensional flow, variable density flow, and compressible reacting flow.

The growth of a sinusoidal perturbation on an infinite shear layer is shown in figure 1a in terms of all the vortex elements used in the

simulation and their velocity vector. Figure 1a illustrates the adaptivity of the scheme; more elements are introduced to capture the straining layers. The growth of small perturbations in a spatially developing shear layer in which the flow was assumed to be semi-infinite is depicted figure 2 in terms of the vortex element distribution. In both the temporal and spatial shear layers, numerical results for the growth rate of small perturbations as a function of the perturbation wavelength were found to agree with the results of the linear stability theory. The nonlinear regime of these Kelvin-Helmholtz instabilities is characterized by the formation of large-scale structures due to the roll-up of the vorticity layer, as shown in figures 1 and 2. Results in this regime are checked for convergence and against experimental data. Convergence is tested by establishing the grid independence of the solution, and whether the solution satisfies certain differential and integral constraints, such as the conservation of vorticity along a particle path, $d\omega/dt = 0$.

Figures 1 and 2 show that beyond the linear range of the instability, where the growth is exponential, the mean growth rate of the shear layer reaches a constant value, in agreement with experimental data. Within this range, the computed results were used to evaluate the flow statistics. Figure 3 shows the close agreement obtained between the computed results and the experimental measurements. We note that mean velocity profiles reach self-similarity earlier than mean fluctuations. The response of the layer to time-dependent boundary conditions was analyzed by modulating the inlet flow at frequencies different from the natural shedding frequency. Samples of the results, in which the flow is forced at the fundamental alone, and at the fundamental and the subharmonic at the same time, are shown in Figures 2b and 2c, respectively. The shear layer growth, and the

accompanying rate of mixing, is enhanced by inducing an earlier shedding, and pairing in the second case, through the application of external forcing [7]. Multiple pairing can be achieved by lower frequency forcing, as discussed in [13].

In a two-dimensional flow, the source of fluctuation is the formation, growth, and pairing of the large-scale vortex structures due to the natural flow instability. Two instabilities are observed in figure 2, the roll-up instability which leads to the formation of large eddies, and the pairing instability which is responsible for the amalgamation of these eddies downstream. We call these the primary instabilities since they grow in the primary, streamwise direction. Forcing, which can be used to either promote or suppress these instabilities, was shown to have a direct impact on the values and signs of these fluctuations, suggesting that by employing carefully designed forcing functions, one can control the interactions between the mean flow and the shear-layer flow [13]. Computations of the initial stages of a two-dimensional turbulent jet were presented in [14].

III. THE VORTEX ELEMENT METHOD IN THREE DIMENSIONS

The vorticity transport equation in an incompressible, three-dimensional, inviscid flow is:

$$\frac{\partial \omega}{\partial t} + \mathbf{u} \cdot \nabla \omega = \omega \cdot \nabla \mathbf{u} \quad (5)$$

where $\omega = \nabla \times \mathbf{u}$, and $\nabla = (\partial/\partial x, \partial/\partial y, \partial/\partial z)$. In this case, $\mathbf{u} = (u, v, w)$ and $\mathbf{x} = (x, y, z)$. The Lagrangian form of Eq. (5) is $d\omega(\chi(\mathbf{X}, t), t)/dt = \omega(\chi(\mathbf{X}, t), t) \cdot \nabla \mathbf{u}$, where $\nabla \mathbf{u}$ is the strain tensor $\partial u_i / \partial x_j$. An equivalent expression which can be used to determine the vorticity directly is the Helmholtz theorem: $\omega(\chi(\mathbf{X}, t), t) = \nabla \chi(\mathbf{X}, t) \cdot \omega(\mathbf{X}, 0)$, where $\nabla \chi$ is the Jacobian of the flow map, $\partial \chi_i / \partial X_j$. Moreover, it can be shown that $\mathbf{u}(\mathbf{x}, t) = \int \mathbf{K}(\mathbf{x} - \mathbf{x}') \times$

$\omega(\mathbf{x}') d\mathbf{x}'$, where $\mathbf{K}(\mathbf{x}) = -1/4\pi \mathbf{x}/r^3$, which is the Biot-Savart law in three dimensions. This Lagrangian formulation is the basis for the construction of three-dimensional vortex methods [15,16].

III.1. NUMERICAL SCHEME

Vorticity is discretized among volume elements, of side h , initially centered around \mathbf{X}_i , by collocation. The vortex elements are then moved along particle trajectories, $\mathbf{X}_i(\mathbf{X}_i, t)$, while their vorticity is changed according to the right-hand side of Eq. (5). Thus,

$$\omega(\mathbf{x}, t) = \sum_{i=1}^N \omega_i(t) h^3 f_\delta(\mathbf{x} - \mathbf{X}_i(\mathbf{X}_i, t)), \quad (6)$$

where in this case, $f_\delta(\mathbf{x}) = 1/\delta^3 f(r/\delta)$ and the rest of the parameters are defined as before. Note that, here, one defines strongly overlapping vortex balls of diameter δ , and that the core function is spherically symmetric, while the vorticity vector associated with an element is ω_i .

The total vorticity vector of an element, $\omega_i h^3$, is expressed more naturally in terms of Γ_i and δl_i where $\Gamma_i = \omega_i h^2$ is the circulation of the element, which remains constant along a particle path in an inviscid flow (Kelvin's theorem), and δl_i is the length of the material element along the vortex line, $\delta l_i = h_i \omega_i / \omega_i$, that changes as the material lines stretch (Helmholtz theorem). The formulation in terms of $(\delta l, \Gamma)$ offers a natural regridding method which is used when $\delta l > \beta h$ due to stretch. In this case, a vortex element is divided into two elements along the vector δl , while preserving the value of Γ . The conditions necessary for the accurate discretization of the initial vorticity in two dimensions are valid in three dimensions, e.g., $\delta > h$. This condition must be satisfied at all time.

The velocity field induced by the discrete vorticity distribution is obtained by substituting Eq. (6) into the Biot-Savart law and integrating. The results can be written as

$$\mathbf{u}(\mathbf{x}, t) = \sum_{i=1}^N \Gamma_i \delta l_i(t) \mathbf{K}_\delta(\mathbf{x} - \mathbf{X}_i(\mathbf{X}_i, t)), \quad (7)$$

and

$$\frac{d\mathbf{X}_i}{dt} = \mathbf{u}(\mathbf{X}_i(\mathbf{X}_i, t), t), \quad (8)$$

$$\delta l_i(t) = \frac{1}{2} (|\mathbf{X}_{i+1}(\mathbf{X}_{i+1}, t) - \mathbf{X}_{i-1}(\mathbf{X}_{i-1}, t)|). \quad (9)$$

where $\mathbf{K}_\delta(\mathbf{x}) = \mathbf{K}(\mathbf{x}) \kappa(r/\delta)$ and $\kappa(r) = 4\pi \int_0^r f(r') r'^2 dr'$. To reduce the computations, we utilize the fact that vortex lines are also material lines in an inviscid flow. Application of Eq. (9) requires maintaining data on the immediate neighbors in the direction of vorticity. Thus, one-dimensional Lagrangian grids are employed to describe individual vortex lines as arrays of vortex elements arranged along the vortex line. The condition that a vorticity field in a three-dimensional free space be solenoidal, $\nabla \cdot \boldsymbol{\omega} = 0$, is implicitly satisfied in Eq. (9). Equations (7)-(9) describe the vortex filament method [17].

III.2. PROPAGATION AND INSTABILITY OF VORTEX RINGS

Before describing their properties, we mention that vortex rings, in addition to providing a test problem for the numerical scheme, play an important role in combustion theory and practice. We refer the reader to the experimental literature for studies on flame-vortex-ring interactions [18] and the large-scale structure of jet diffusion flames [19].

It has been shown analytically that the self-induced velocity of a thin vortex ring, $\sigma \ll R$, where σ is the core radius and R is the ring radius, is

a function of σ/R and the vorticity distribution within the core, $\Omega(r/\sigma)$ [20]. Numerically, using $\delta = \sigma$, the dependence of the self-induced velocity on σ/R was accurately computed when overlap was maintained between neighboring vortex elements along the ring axis [21]. The long-wave azimuthal instability of a thin vortex ring, with a wavelength $\lambda \gg \sigma$, was observed when the ring was perturbed along its axis with a number of waves $n = 2\pi R/\lambda$. The computed unstable wavenumber, $k^* = 2\pi/n^*$, and growth rate of these waves within the linear range agreed with the prediction of the corresponding linear theory [22]. The growing standing waves at k^* , contrary to the spinning stable waves at all other wavenumbers, expend the flow energy in stretching the waves in the direction opposite to the ring self-induced velocity.

In the nonlinear range, the growing waves form almost closed loops of vorticity behind the original ring, as shown in figure 4. These loops are connected to the original ring via very narrow necks that can be pinched off by the action of viscosity. Each loop is formed of two vortex rings of opposite signs of vorticity separated by a very small distance. The separation of these loops from the parent ring may lead to the formation of off-spring vortex rings with a smaller diameter than that of the original ring. This would result in an interesting cascading to smaller scales; a faster decay of the original ring; and the reduction of the circulation of the parent ring [23].

The study was extended to investigate the growth of short-wave instabilities, $\lambda \sim \sigma$, within the core of the ring. In this case, one must allow the core of the ring to deform under the action of the growing perturbation. Analysis of variations within the core requires adequate resolution of its vorticity field by utilizing vortex elements with a core

radius $\delta < \sigma$, i.e., several elements must be used to accurately describe the vorticity field within the core. The computed value k^* , shown in figure is in close agreement with the prediction of the linear theory for short-wavelength instability in deformable vortex rings. The value of k^* depends on the vorticity distribution within the ring core, $\Omega(r/\sigma)$. figure 5 shows that the value of k^* , predicted from the short-wave analysis, is closer to the experimental data than that predicted by the previous long-wavelength.

Spectral analysis of the field of an unstable ring shows that as the fundamental instability reaches saturation, its harmonic becomes unstable and starts to grow. The mechanism of excitation of this frequency, displayed in figure 6, is associated with the formation of hairpin vortices at half the wavelength of the original perturbation. Examining the vorticity field after the saturation of the first instability reveals the presence of a strong streamwise vorticity component with alternating signs as one moves along the axis of the original ring [24]. This component is the result of the tilting of the original vortex lines into the streamwise direction. The tilting occurs as the azimuthal instability grows. Within each azimuthal wave, two vortices of opposite signs are formed.

The scheme was also used to study the three-dimensional instability of the initial stages of an axisymmetric jet [17]. It was found that the jet rolls up into vortex rings which experience a similar instability to that of an isolated vortex ring.

III.3. SECONDARY INSTABILITIES OF SHEAR FLOW.

Beyond the primary instability, shear flows develop secondary instabilities which leads to the generation of streamwise vorticity (the vorticity vector points in the streamwise direction), an important mechanism of mixing enhancement [24-26]. To simulate this process, the shear layer is

initially perturbed in the streamwise and spanwise directions, and the vortex scheme is modified to accommodate the strong strain field which develops in the plane normal to the initial vorticity. This is accomplished by redistributing the vorticity field among a larger number of elements arranged in the direction of maximum strain.

In the transport element scheme, each vortex element is defined by its circulation and two material vectors: one in the direction of vorticity and the other in the direction of maximum strain. This is equivalent to using two-dimensional Lagrangian grids to describe planes of constant circulation. The stretch of the sides of the grid can be used to update the vorticity associated with each element in the plane. Alternatively, a grid-free stretching scheme can be constructed on the basis of Eq. (5). In this scheme, the term $\omega \cdot \nabla u$ is computed for each element by analytically differentiating the velocity expression in Eq. (7). The computational effort is almost the same in both schemes, however the bookkeeping in the first scheme is greater [26].

The evolution of a temporal shear layer is displayed in the next three figures. Figure 7 depicts the distortion of the material surface initially aligned along the midsection of the layer, where $u = 0$, in terms of the two-dimensional grid used to discretize its vorticity (this is one of several such surfaces used to discretize the vorticity). Figure 8 shows the distribution of the streamwise vorticity contours on a y - z streamwise plane (a streamwise plane is normal to the streamwise direction) which cuts through the core of the spanwise structure at the middle of the domain. Figure 9 depicts the streamwise vorticity on a y - z plane which cuts through the braids of the spanwise structures (the principal axis of this structure coincides with the spanwise direction). The distribution of the streamwise

vorticity indicates that during the growth of the streamwise perturbation, the growth of the spanwise perturbation is suppressed, and the flow remains almost two-dimensional. The growth of the streamwise instability (not shown) matches that of a two-dimensional flow until the time the streamwise instability saturates, $t = 8$. The saturation is accompanied by the formation of a spanwise, circularly shaped vortex core whose axis is perpendicular to the mean flow direction. The formation of this core is accompanied by a secondary flow whose streamlines are almost circular.

Beyond the saturation of the streamwise instability, $t > 8$, the growth rate of the spanwise instability increases and the vortex core starts to deform. This deformation, and the concomitant tilting of the vorticity vectors from the spanwise direction into the streamwise direction, leads to the establishment of a streamwise vorticity component with an alternating sign along the axis of the spanwise cylindrical structures. The deformation of the spanwise cylindrical cores is known as the translative instability. The streamwise vorticity associated with this instability is shown in figure 8. The fact that the cores are covered from both sides by two rows of streamwise vortex rods is explained next.

The other source of streamwise vorticity is the deformation of the vortex lines of the braids in the cross-stream direction, as shown in figure 7. The vorticity component in the cross-stream direction is transformed into a streamwise component by the action of the velocity gradient, $\partial u / \partial z$, where u is the velocity component in the x -direction. Along the spanwise direction, streamwise vorticity changes its sign every half wavelength. This configuration is unstable, and each half wavelength rolls up to form a vortex rod aligned with the local direction of the braids, as shown in figure 9. The vorticity within these rods is constantly amplified as the

strain field in the streamwise direction, generated by the large spanwise cores, strains the flow along the direction of the braids. With elongation, these rods wrap around the spanwise cores and produce the distribution shown in figure 8.

The deformation of the flow field due to the evolution of the two and three-dimensional instabilities leads to a substantial enhancement of mixing within the large structures by generating strong entrainment currents of fluids from both sides of the shear layer towards the vortex center. The mixing enhancement, and its effect on the burning rate are discussed in detail in the next sections.

IV. THE TRANSPORT ELEMENT METHOD

Given that s is a passive, nondiffusive scalar, the conservation equations for s , and $g = \nabla s$, in an incompressible flow are:

$$\frac{ds}{dt} = 0, \quad (10)$$

and

$$\frac{dg}{dt} = -g \cdot \nabla u - g \times \omega. \quad (11)$$

Thus, s remains constant along a particle path, while g changes due to the straining and rotation of the material lines by the local strain field and vorticity. If the material is exposed to a strong strain in the direction normal to the gradient, the value of g must increase by the same amount as the stretch in the material element. This can be seen by deriving an explicit equation which relates the changes in $g = |g|$ to the variation of material elements, or the distortion of the flow map. This is done by expanding Eq. (11) in terms of $g n$, and implementing kinematical relations that describe the variations of $n = g/g$, where n is the unit vector normal

to an isoscalar line, i.e., a line along which s is constant. After some lengthy manipulations, we get:

$$\frac{dg}{dt} \mathbf{n} = -g (\mathbf{n} \cdot \nabla \mathbf{u} + \frac{1}{2} \mathbf{n} \times \boldsymbol{\omega} - (\mathbf{l} \cdot (\mathbf{n} \cdot \nabla \mathbf{u}^S)) \mathbf{l}), \quad (12)$$

where $\nabla \mathbf{u}^S$ is the symmetric part of the strain tensor $\nabla \mathbf{u}$ and \mathbf{l} is the unit vector normal to \mathbf{n} . Moreover, $g = (ds/dn) \mathbf{n} \sim (\delta s / \delta n) \mathbf{n}$, where δs is the variation of s across a small material line δn . In two dimensions and for an incompressible flow, the variation of a material vector element $\delta \mathbf{l}$ can be shown to be governed by a similar equation to Eq. (12).

IV.1. NUMERICAL SCHEME.

From the above discussion on the relationship between scalar gradients and the deformation of the flow map, it follows that $g/\delta \mathbf{l} = \text{constant}$ along a particle path, and that the scalar gradient can be computed from the following relations [7]:

$$g(\mathbf{x}, t) = \sum_{i=1}^N g_i(t) h^2 f_{\delta}(\mathbf{x} - \chi_i(\mathbf{x}_i, t)), \quad (13)$$

where

$$g_i(t) = \frac{\delta s_i \delta \mathbf{l}_i(t)}{h^2} \mathbf{n}_i(t), \quad (14)$$

and $\chi_i(\mathbf{x}_i, t)$ is, as before, a particle path. Equation (13) is based on the expansion of g in terms of the core function f_{δ} , similar to Eq. (2). Since an isoscalar line is a material line in a nondiffusive field, $\delta \mathbf{l}_i$ can be updated as: $\delta \mathbf{l}_i(t) = (\chi_{i+1} - \chi_{i-1})/2$, while $\mathbf{n}_i \cdot \mathbf{l}_i = 0$. Thus, it suffices to move the centers of the transport elements while remembering the near neighbors at $t = 0$. As in the vortex method, when the distance between neighboring elements in the direction of maximum strain exceeds a certain maximum, an element is inserted between two neighboring elements. The total

of δl_i 's for the two original elements are distributed among the three elements, while h^2 and δ^2 are adjusted so that the total material area is conserved, keeping δs_i the same.

For a variable-density flow, the above analysis is modified to reflect the fact that, in this case, an equation similar to Eq. (12) can be derived with g replaced by $\rho \delta l$, and the expression of g_i in Eq. (13) changes to [12,27]:

$$g_i(t) = \frac{\delta s_i \delta l_i(t) \rho_i(t)}{\rho_i(0) h^2} n_i(t). \quad (15)$$

The value of ρ is computed using the relation $\rho T = \text{constant}$ in the low Mach number approximation (see Section V). Given the location and strength of the transport elements, the scalar concentration are computed by direct integration over the fields of the transport elements

$$s(x,t) = \sum_{i=1}^N g_i(t) h^2 \cdot \nabla G_\delta(x - X_i(X_i, t)), \quad (16)$$

where, in two dimensions, $\nabla G_\delta(x) = (x,y)/2\pi r^2 \kappa(r/\delta)$, and in three dimensions, $\nabla G_\delta(x) = (x,y,z)/4\pi r^3 \kappa(r/\delta)$. This formulation is fully compatible with the vortex method since all the information needed to compute the scalar transport are already part of the vortex computations, including all the expressions of the Green functions. For extended derivations, see [24,27].

The effect of molecular diffusion in the vortex and transport element methods can be modeled by expanding the cores of the elements according to the following relation, $\delta^2(t+\Delta t) = \delta^2(t) + 2 \alpha \Delta t$, where Δt is the time step and α is the molecular diffusivity [6]. This relation is obtained by direct substitution of Eq. (11) into the diffusion equation. A limit should be

imposed on the maximum allowable value of δ to maintain the spatial accuracy of the calculations. Beyond δ_{\max} , an element should be subdivided into a number of smaller elements. Another scheme for implementing the effect of diffusion without expanding the cores was proposed in [28]. This scheme is used in conjunction with the three-dimensional transport element method in Section IV.3.

IV.2. SCALAR MIXING IN SHEAR LAYER

The transport element method was used to study the transport of species in a two-dimensional, heterogeneous shear layer [12]. Figure 1b shows the isoscalar lines of the shear layer of figure 1a when the diffusivity is zero. Numerically, we found that, provided the field is accurately discretized initially, the condition $ds/dt = 0$ is satisfied if the core radii of the elements are allowed to decrease at the rate described in Section II, i.e. if h^2/δ^2 remains constant as the elements are deformed. This also guarantees that the scheme can capture, without introducing numerical diffusion, the large scalar gradients that arise from the strong deformations in the flow which accompany the evolution of the instability.

Figure 10 shows a comparison between the computed and the measured values of the mean concentration and the root-mean square of the concentration fluctuations in the two-dimensional spatially developing mixing layer of figure 2a [12,29]. The computational results were obtained for a range of Peclet number between 10^3 and 10^5 , so that the dominant transport process was convection and not diffusion. However, the effect of species diffusion was incorporated to study mixing. The effect of diffusion on the mean scalar distribution is very small since the overall concentration field is established by the convective field, also called the entrainment currents. Due to the roll-up of the vorticity layer, fluid from

both sides of the shear layer are engulfed into the large structure and, on the average, mean values, between the two extremes, can be encountered.

The root-mean square of the concentration fluctuations exhibit strong dependence on the Peclet number. Its maximum value, 0.5, can only be achieved at very high Peclet number where strong unmixedness is present inside the cores of the eddies. As the effect of molecular diffusion increases, it homogenizes the cores and the fluctuations drop below 0.5. In this case, the profiles show a mixed region of constant value of fluctuation. For all values of the Peclet number, the fluctuations never reached zero inside the cores indicating that the fluid does not reach complete homogeneity. Another interesting feature of these mixing flows, is the presence of more high speed fluid than low speed fluid inside the cores [12]. This mixing asymmetry, which is a direct consequence of the unequal velocities across the interface of the layer, will be shown to play an important role in the distribution of products.

IV.3. ENTRAINMENT ENHANCEMENT DUE TO 3D INSTABILITIES

The three-dimensional transport element method is based on the relationship between the distortion of the flow map and the scalar gradients, as in the two-dimensional method. In 3D, the distortion of the flow is represented by the changes in the magnitude and direction of a material area element initially aligned with an isoscalar surface ∂A . This relationship was derived in [24,30] for a variable density flow;

$$\frac{d}{dt} \ln g = \frac{d}{dt} \ln (\rho \delta A). \quad (17)$$

Equation 17 indicates that $g/(\rho \delta A) = \text{constant}$ along a particle path. To implement this relationship in the calculations of the scalar gradients, one must keep track of the area of the elements associated with computational

points moving along particle trajectories. Similar schemes are used in the vortex element method to monitor the effect of the strain field on the evolution of the vorticity field. Thus, the computation of the scalar transport is a natural extension of the vortex element method since it does not require additional computational effort.

The entrainment due to the development of three-dimensional instabilities in shear flow is depicted in figures 8 and 9 where we show the scalar contours on the same planes where the streamwise vorticity contours are displayed. The extra entrainment, over what is observed in two-dimensional calculations, is induced by the action of the spanwise deformation of the vortex core and by development of the streamwise vortex rods within the braids, as shown in figures 8 and 9, respectively. The total entrained fluid within the large eddies is measured by the size of the eddy in the cross-stream direction, and shown in figure 11 for both the two and the three-dimensional calculations [24,26]. The effect of this extra entrainment on the rate of burning will be discussed in Section VI.2.

V. VORTEX METHODS FOR VARIABLE-DENSITY FLOWS

In combustion phenomena of practical interest, the flow is density stratified, i.e. finite and large density gradients exist between material layers, due to heat release and the variation in molecular weight of reacting species. The effect of density gradients is to introduce a baroclinic source term in the vorticity transport equation. In this section, we show how this term is included in the simulation, and describe its effect on shear layers. Considering an incompressible, inviscid, variable density, the conservation equations are:

$$\frac{d\rho}{dt} = 0, \quad (18)$$

$$\frac{d\omega}{dt} = \frac{1}{2} \nabla \rho \times \nabla p + \omega \cdot \nabla u, \quad (19)$$

where $\nabla p = -\rho \, du/dt$ and ∇p is computed using the transport element method as described before. Extensions to gravity-driven at finite Froude number are considered in [27,31]. To take the extra term in Eq. (19) into account, the computational algorithm proceeds in fractional steps: (1) the vorticity is transported without change along the particle trajectory, Eq. (8); (2) the material acceleration along the particle path is computed to find the pressure gradient; (3) the change in the density gradient along the particle path is evaluated using the transport element method, Eq. (14); and (4) the vorticity is updated according to the discrete analog of Eq. (19),

$$\frac{d\Gamma_i}{dt} = - \frac{\nabla \rho_i}{\rho_i} \times \left(\frac{du}{dt} \right)_i h_i^2. \quad (20)$$

V.1. BAROCLINIC EFFECTS IN SHEAR LAYER.

Computations of a variable density shear layer were performed to investigate the effect of baroclinic vorticity generation on the growth rate of the Kelvin-Helmholtz instability, the rate of entrainment and the rate of expansion of a shear layer. Figure 12 shows a sample of a two-dimensional simulation in which the fast top stream is five times heavier than the slow bottom stream. This configuration resembles the experimental set-up used to study a shear layer between premixed reactants moving in the top stream and products of combustion moving in the bottom stream [34]. The computed initial growth rate and phase velocity of the growing waves compared well with the results of the linear stability theory [12, 35].

In the nonlinear range, the computational results indicate that density variation: (1) induces a net convective motion on the eddy in the direction of the heavy stream; (2) enforces entrainment asymmetry on the growing eddy

which results in the presence of more light fluid than heavy fluid, by volume, within the core; and (3) destabilizes the flow leading to the formation of large scale structures within the large scale structure. It was also observed that baroclinic vorticity enhances entrainment over that of the uniform-density case. Using a Galilean transformation between the temporal and spatial shear layer, i.e., $d\delta/dx = 1/U_c d\delta/dt$ where u_c is the finite convective velocity, one can show that a shear layer in which the heavy stream moves faster than the light stream will grow more slowly in the streamwise direction than a uniform density layer, in agreement with experimental observations [36].

Similar changes were found in the results of a three-dimensional simulation of a variable density flow. Figure 13 shows a sample of these results for the case of a top, fast stream is twice as heavy as the bottom, slow stream [30]. The results are represented by the grid used to describe the material surface initially aligned with the midsection of the shear layer, as in figure 7. The motion of the developing eddy, its asymmetry with respect to the top and bottom streams and some added asymmetry in the spanwise direction are clearly seen in the figure. Secondary instabilities, leading to the deformation of the spanwise core and the formation of streamwise vortex rods within the braids, are similar to those encountered in the two-dimensional simulations.

The dynamic origin of these phenomena is the generation of vorticity due to the baroclinic torque. The misalignment of the density and pressure gradients within the growing eddy leads to the generation of additional vorticity with two opposite signs on the two sides of the shear layer, as shown in figure 12. In the case considered here, vorticity of a similar sign as that of the shear layer is generated on the light, slow fluid side

while vorticity of the opposite sign is generated on the fast, heavy fluid side. This redistribution of vorticity within the growing eddy leads to more entrainment from the lower, light fluid side of the layer and a net streamwise motion of the large eddy in the direction of the heavy fluid. The computed entrainment ratio and finite eddy velocity were found to agree with experimental results [32]. In Section VI.4, we show how baroclinic vorticity generation affects combustion in premixed shear layer.

The effect of baroclinic vorticity on the instability of a jet was presented in [14], without and with the effect of Froude number. The role of baroclinic vorticity in determining the structure of low-speed jet diffusion flames is analyzed in [27]. The extension of the calculation of a variable density flow to a premixed shear layer, and the corresponding role of baroclinic vorticity are discussed in Section VI.4.

VI. VORTEX METHODS FOR REACTING FLOWS

The transport element method was extended to reacting flow [7,35,37]. In combustion systems, heat release at low Mach number leads to the generation of an irrotational velocity field, $\nabla\phi$, which when superimposed on the existing vorticity-induced rotational velocity, u_ω , represents the total velocity in a reacting flow. The low Mach number approximation is employed to filter out the pressure waves and to render the pressure independent of the density in unconfined flows [38]. Employing the velocity decomposition, the governing equations of combustion can be written as follows:

$$u = u_\omega + \nabla\phi, \quad (21)$$

$$\nabla^2\phi = \frac{1}{T} \frac{dT}{dt}, \quad (22)$$

$$\frac{d\omega}{dt} = \frac{1}{\rho} \nabla\rho \times \nabla p - \omega (\nabla \cdot u) + (\omega \cdot \nabla) u + \frac{1}{Re} \nabla^2 \omega, \quad (23)$$

$$\frac{dT}{dt} = \frac{1}{P_e} \nabla^2 T + Q W, \quad (24)$$

$$\frac{dc_k}{dt} = \frac{1}{P_e L_e} \nabla^2 c_k + W_k, \quad (25)$$

$$\rho T = \text{constant}, \quad (26)$$

where T is temperature, c is species concentration, W is the rate of creation/destruction of species, Q is the enthalpy of reaction, R_e , P_e and L_e are the Reynolds, Peclet and Lewis numbers, respectively. Here, we assume that (1) the transport properties are constant except for mass diffusivity which is replaced by a density-averaged value; and (2) molecular weights of reactants and products are the same. The pressure gradient is obtained from the momentum equation: $\nabla p/\rho = -a + 1/(\rho R_e) \nabla^2 u$, where $a = du/dt$. Both velocity components, u_ω and $\nabla\phi$ must satisfy the velocity boundary condition in the direction normal to the boundaries of the domain. Using the principle of vortex decomposition, i.e., discretizing the source term in Eq. (22) in a form similar to Eq. (2), Green's function solution of Eq. (22) can be written as [7]:

$$\nabla\phi(x,t) = \sum_{i=1}^N \frac{1}{T_i} \left(\frac{dT}{dt} \right)_i h_i^2(t) \nabla G_\delta(x-X_i(X_i,t)). \quad (27)$$

The energy equation and the species transport equations, Eq. (24) and (25), respectively, are solved using the transport element method in three fractional steps: convection, diffusion and reaction. The reaction fractional step is implemented by changing the strength of the transport elements according to the following expression [7]:

$$\frac{d}{dt} \delta s_i = \sum_{j=1}^{k+1} \frac{dW}{ds_j} \delta s_j, \quad (28)$$

where k is the total number of species and $s_{k+1} = T$.

In the following, we review four solutions of reacting shear layers, computed using the transport element methods. The first three solutions are obtained for the reaction between two streams of fuel and oxidizer, and the fourth is for a reaction between a stream of premixed reactants and a stream of products. In the first two cases, an incompressible flow model was used to eliminate the complexity of the effect of heat release on the flow dynamics. In the third and fourth cases, a compressible flow model was used. In all cases, we focus on the mechanisms of shear flow-combustion interactions under different physical conditions.

VI.1. THE REACTING SHEAR LAYER

A computation of a reacting shear layer between a fuel stream, F , and an oxidizer stream, O , in a spatially developing flow was described in [39,40]. The incompressible flow model, $\rho = \text{constant}$, was used to investigate how the flow which evolves due to the roll-up instability affects the combustion process. The chemistry is modeled by one-step reaction kinetics, $F + O \rightarrow P$, and the reaction rate is taken as $W = A_f c_F c_O \exp(-T/T_a)$, where A_f is the frequency factor and T_a is the activation energy normalized with respect to the gas constant. A sample of the results, obtained for $T_a/T_R = 10$, $A_f = 8000$ and $Q = 1$, is shown in figure 14, revealing a strong similarity between the temperature, product concentration and the vorticity contours, being highest within the cores and reaching very small values within the braids. A large eddy, defined by a closed set of vorticity contours, figure 14c, can also be described by a set of closed product concentration contours, around the same origin and of the same shape as the vorticity contours, figure 14b. This similarity confirms the important role of advection, which is governed by vorticity in this case, in

determining the local concentration field, the rate of mixing and the rate of burning.

The effects of the shear layer roll-up, the Damkohler number, Reynolds number and reactants ratio across the layer are shown in figure 15. These results were obtained for a temperature-independent reaction in which $W = D_a c_F c_P$, where D_a is the Damkohler number. The roll-up of the shear layer enhances product formation over the laminar layer by inducing strong entrainment currents into the cores. A drop in the total product formation in the early stages is due to the thinning of the reaction zone by the strain field. Product formation depends strongly on the Damkohler number. This dependence, however, vanishes and the total amount of product formed within the layer reaches an asymptotic value at Damkohler number on the order of 20, based on the length scale of the large structures. This is the fast chemistry limit at which the rate of product formation depends only on the mixing rate.

At high Reynolds numbers, of an order of 10000 based on the length scale of the large eddies, product formation is a weak function of the Reynolds number. This indicates that while mixing is strongly enhanced by convective entrainment, it is also globally limited by it. The mechanism of this apparent double role is explained as follows. When the Reynolds number is high, diffusion between the reactants occurs across a highly convoluted interfacial layer embedded within the large structures at a much faster rate than the entrainment of the reactants into the large eddies. Thus, changing the diffusion rate by varying the Reynolds number does not affect the product formation since the process is entrainment limited.

The phenomenon of mixing asymmetry, which arises due to the finite velocity difference between the two streams [7], is shown in the product

distribution in figure 14b, and is manifested in the dependence of the product formation of the reactants ratios in figure 15c. The reactants ratio is defined as the ratio between the two reactants concentrations across the layer. For equal concentrations of reactants in the two streams, the average product concentration in the lower, slower stream is persistently higher than in the upper, faster stream. This is because the large structures entrain more high-speed than low-speed fluid. The bias towards the entrainment of the high-speed stream results in a faster chemical reaction in the lower section of the layer than in the upper section. Increasing the concentration of either reactants enhances the rate of product formation since the chemical reaction becomes faster. However, to improve the overall rate of burning, it is more effective to increase the slow-stream concentration to compensate for the entrainment asymmetry.

VI.2. 3D REACTING SHEAR LAYERS.

We have shown in Section III.3 that three-dimensional secondary instabilities follow the saturation of the two-dimensional instabilities. The complicated mixing patterns, which arise due to the evolution of three-dimensional instabilities in shear layers, are revealed by the results of a reacting flow simulation between a stream of fuel and a stream of oxidizer [30]. Figure 16 shows product concentration and reaction rate contours on (a) a spanwise x-z section which passes through the midsection of the domain of figure 7; and (b) and (c) the two streamwise y-z sections used to depict vorticity in figures 8 and 9. An incompressible, temporal, periodic flow model, and a reaction rate $W = D_a c_O c_F$, are used. The physical parameters are: $D_a = 10$, $P_e = 1000$ and $L_e = 1$. We only show the late stages when three dimensional effects become important.

These figures show an unexpected inhomogeneity of mixing, and combustion inside the cores in the streamwise and the spanwise directions, even at the late stages of instability development. As mentioned before, these flows are entrainment dominated. The mixing between the two streams is initiated along convoluted interfaces which are produced by the uneven stretch within the large structures. The stretch is a consequence of the vorticity instability. Diffusion, a process much slower than convection at high Reynolds number, occurs within these thin, convoluted zones. The chemical reaction at $D_a = 10$ converts mixed reactants into products almost immediately. Thus, products are formed within thin convoluted zones embedded inside the large structures.

In two-dimensional simulations, products are found inside the large cores. In three-dimensional simulations, products are found within the large cores and within the braids due the formation of the rods. In both cases, zones of maximum strain in the spanwise and streamwise planes are depleted of products by mechanisms which will be discussed next section. Thus, 3D simulation confirm our earlier observation that product concentration is maximum where vorticity concentration is highest, and that at zones of high strain and small vorticity, product concentration is lowest. This correlation holds at all times and across all sections. This correlation has been observed in the spanwise plane in several two-dimensional computations [40]. In the streamwise planes, the correlation between vorticity and product concentration is supported by figures 16b and c; and figures 8 and 9.

The dynamic origin of this correlation is revealed by inspecting the reaction rate contours shown in figure 17. At the early stages, products form at the center of the eddies where mixing occurs due to the entrainment

field. Later, reaction is maximum at the outer edges of the structure. Thus, at this high value of D_a , product formation zones move from the center of the core to the outer edges of the eddies. However, at all stages, the entrainment field draws the products towards zones of maximum vorticity which exist inside the cores and the rods. Thus, although products may form away from the zone of maximum vorticity, they are constantly brought there by the convective field.

The reaction zone does not exhibit a similar correlation with the vorticity. It has, thus, been suggested that vorticity be used as a primary variable in turbulent combustion models [41].

VI.3. THE REACTING JET.

The effect of exothermic energy on the flow dynamics and the structure of the reaction zone was investigated in the case of a reacting jet of fuel issuing in an atmosphere of oxidizer [27,42]. The flow is two-dimensional and planar and the jet forms two vorticity layers with two opposite signs on both sides of its centerline. We used a compressible flow model, Eqs. (21)-(26), and a single step Arrhenius reaction, $W = A_f c_F c_O \exp(-T_a/T)$. Figure 17 depicts the product distribution for $A_f = 150$ and 750. Both were obtained at $P_e = 1000$, $L_e = 1$, $T_P/T_R = 4$, $Q = 3$, and $T_a/T_R = 10$. The initial perturbation amplitude is $\epsilon = 0.05 \lambda$, where λ is the wavelength in the streamwise direction. Figure 18 shows the reaction rate contours for the two cases.

VI.3.1. PRODUCT DISTRIBUTION

At high Damkohler number, product concentration is higher due to the faster chemical reaction, and the eddies are larger due to the extra heat release, as shown in figure 16. At both values of D_a , product concentration within the shear layers changes from a uniform distribution in the

streamwise direction to a highly-concentrated distribution within the large eddies as the flow evolves. Product concentration within the braids, however, decreases continuously. The thinning of the braids, due to the formation of a strong strain field as the eddies roll-up, reduces the zones of overlap between the jet and oxidizer fluids, of the zone of chemical activity. Moreover, the large relative velocity between the jet and oxidizer streams within the braids also reduces the time available for mixing within this region. Finally, the entrainment currents convects products forming within the braids into the cores leading to continuous cooling of the region between neighboring eddies. This the physical mechanism of reaction extinction within the braids. Clearly, it is convection-driven.

The similarity between product distribution and vorticity, observed in Section VI.1, persists in the case of a reacting jet, both at low and high Damkohler number. Both product concentration and vorticity exhibit high values within the eddies and fall continuously along the braids. Thus, vorticity still controls product distribution within the eddy. At high Damkohler number, vorticity produces a swirling field that enlarges the surface of contact between the two reactants, diffusion mixes them across the stretched surface, and products form. The swirling convective field then entrains these products into the eddy core. At low damkohler number, reactants are entrained into the cores and then react. The difference between the two mechanisms is illustrated by examining the reaction rate contours for both cases.

VI.3.1. STRUCTURE OF THE REACTION ZONE.

At low Damkohler number, reaction rate contours presented in figure 17 show that the zone of chemical activity, initially uniform in the streamwise

direction, is enlarged during the entrainment phase of the eddy. The mixing of jet and ambient fluids, induced by the rotational field within the eddy core, extends the area of combustible mixture. Moreover, the reaction rate inside the eddies increases with time triggered by the acceleration of the chemical reaction as the temperature rises due to the formation of more products. Large eddies, thus, act as exothermic centers that support combustion. At this low Damkohler number, an eddy acts as "mixture preparation zone" before combustion proceeds. This is consistent with the fact that the rotational flow within the eddy occurs at a smaller time scale than the chemical reaction.

At high Damkohler number, the reaction zone differs substantially from that at low Damkohler number. At early stages, the reaction rate is maximum inside the eddy where combustion occurs over a distributed zone. In this case, both reactants are drawn into the mixing zone within the eddy core before they combust. At late stages, combustion occurs on the outer edges of the eddies within a thin reaction zone. Now, reactants coexist only around the outer edges of each eddy where they react and form products which are then entrained into the eddy core. Note that with finite-rate kinetics, and with low-temperature reactants at the early stages, there is an ignition delay which keeps the kinetic rate lower than the mixing rate. As the temperature rises, kinetic rates exceed mixing rates and the reaction region becomes a thin zone between jet and ambient fluids.

At low and high D_a , the reaction rate within the braids drops sharply as the eddies form due to the entrainment of products into the eddy cores (Note that since the Lewis number is unity, temperature and product concentration are similar). Product formation is inhibited within the braids following their cooling by convection.

VI.3.3. EFFECT OF HEAT RELEASE.

In a reacting flow with finite-rate kinetics, we found that heat release reduces that rate of growth of the instability [27] when the initial perturbation is small, $\epsilon = 0.01 \lambda$. The suppression of the instability becomes stronger as the Damkohler number is increased. Similar suppression of instability is observed at infinite-rate kinetics at a range of initial perturbation $\epsilon = 0.01 - 0.05 \lambda$ [42]. In both cases, eddy growth in the direction normal to the jet axis is reduced as the Damkohler number is increased. The reason is as follows: At infinite-rate kinetics, exothermic energy and volumetric expansion start early, within the linear stages of instability growth, forming a sublayer of low-density products within the vorticity layer. Within these stages, it has been shown that the presence of low-density sublayer within the vorticity layer leads to substantial reduction of the instability growth rate [43]. The delay in roll-up results in the formation of a weak, less coherent eddy. Even at finite-rate kinetics with small initial perturbation, an appreciable amount of products forms within the vorticity layer before the instability amplitude is large enough to initiate roll-up. In this case, the early formation of a low-density sublayer of products, embedded within the vorticity layer, precedes the rollup and leads to an overall reduction in the instability growth rate.

At finite-rate kinetic with large initial amplitude, $\epsilon = 0.01 \lambda$, instability suppression is negligible, as seen in Figure 17. Thus, one can overcome the stabilizing effect of volumetric expansion on shear layer growth by forcing the jet at large amplitudes. Initiating roll-up, before measurable volumetric expansion has occurred, causes eddy formation and the onset of mixing enhancement during the ignition delay time. Very small

initial perturbations with high exothermic energy, on the other hand, result in instability suppression.

VI.4. THE PREMIXED SHEAR LAYER

Computations of a shear layer growing between two streams of premixed reactants and products were presented in [7,35]. In this case, the reaction rate, based on one-step reaction kinetics $R \rightarrow P$, is expressed as $W = A_f c_R \exp(-T/T_a)$. Results for a range of Damkohler number and initial amplitude of perturbations are presented. A sample of the results is shown in figure 19 in terms of the rate of reaction, the product concentration, and the vorticity for the case of $T_a/T_R = 10$, temperature ratio $T_P/T_R = 5$, $Q = 4$, $A_f = 1$, $P_e = 1000$ and $L_e = 1$. Figure 20 shows the total mass of products formed within the layer for the same physical parameters but for several values of the Damkohler number. The length of the line of maximum reaction rate, and the total mass of product for a representative case is shown in figure 21. A careful inspection of these results reveal several interesting observations.

Figures 19 and 20 indicate that one can divide the combustion in a premixed shear layer into four phases: (1) a laminar flame; (2) a strained laminar flame; (3) a vortex-driven combustion, (4) a free-propagating flame. In the second phase, the reaction zone in figure 19 is thinner than that of a laminar flame due to the strain, and the total amount of products formed, $M_p = \int \rho c_p dy dx$, is less for the shear layer than for the laminar flame, $M_p = S_u \lambda$ where λ is the perturbation wavelength. In the third phase, the entrainment associated with the formation of a coherent vortex leads to the swelling of the core and the establishment of a reaction zone inside the eddy core. Figure 20 shows that the formation of a vortex core enhances the rate of burning. As the flame leaves the burning vortex, it returns to the

state of a laminar flame. Since these phases result from the interaction between the flow and the chemical reaction, their starting time and duration are strongly dependent on the Damkohler number.

Figure 21 shows that the wrinkled flame model, which states that the rate of product formation $\dot{M}_p = S_u L_f$ where S_u is the laminar burning velocity and L_f is the total flame length, can be used to approximate the burning rate during the initial growth phase of the eddy provided that L_f is measured along the line of maximum reaction rate. However, during the later stages, the value of S_u , as defined above, is found to decrease below the value of the unstrained flame. During the later stages, after most of the eddy core has burnt, it is difficult to define a flame front due to the convolution of the streamlines and further studies of the detail structure of the reaction zone is needed.

Baroclinic vorticity generation, associated with the interaction between the hydrodynamic pressure gradient and density field, contributes to the dynamics of the shear layer in the same way as in the nonreacting, density-stratified shear layer described earlier: the large eddies move in the direction of the cold reactants; entrainment asymmetry biases the composition of the large eddies towards the hot product stream; and local spotiness appears within the large eddy. One difference is clear by comparing figures 12 and 19: heat release slows down the streamwise motion of the large eddies. Due to the volumetric dilatation associated with heat release, the local concentration of vorticity decreases and the induced field on the vortex weakens. Thus, heat release weakens the instability through the mechanism of volumetric expansion and not vorticity generation.

Heat release at high Damkohler number reduces the growth rate of the instability at the initial stages and inhibits the rollup process if the

initial perturbation is small, $\epsilon = 0.01 \lambda$, similar to the reacting jet case. The mechanism of instability suppression in this case is different from that found in the reacting shear layer. In a premixed shear layer, baroclinic vorticity by itself enhances the instability growth rates, as shown before. Volumetric expansion is, thus, necessary for instability suppression in the premixed shear layer flow.

The effect of the Damkohler number on the structure of the reaction zone is similar to the reacting jet; at low Damkohler number, reaction occurs within the eddy core and at high Damkohler number, it occurs primarily on the outer edges of the eddy. As in the reacting shear layer, product concentration is always higher at the center of the eddy (premixed shear layer are however more subtle since product forming during the development of the shear layer and products existing at the initial state are not easily distinguishable). As shown in figure 20, the effect of the shear layer on the burning rate is stronger at low Damkohler number.

VII. EXTENSIONS

Work reviewed so far focuses on combustion in free shear flows. Brief summary of the numerical methodology and its application to nonreacting and reacting shear layer has been presented. Analysis of the computational results aimed at testing the accuracy of the numerical schemes and describing some of the general properties of these flows. In the reacting flow, mechanisms of shear flow-combustion interactions were analyzed in light of the numerical solutions.

The application of vortex methods to internal, wall bounded flows in which the growth of boundary layers along solid walls and their separation at sharp edges play a dominant role in the dynamics of the flow, has been based largely on the random vortex method. In this method, the effect of

molecular viscosity is taken into account by adding a Gaussian random component to the convective motion of the vortex elements [44,45]. Extensive work on the validation of the method [46,47] shows that solutions for steady, low Reynolds number flows, and unsteady, high Reynolds number flows converge to appropriate limits as numerical parameters are refined. Low-Reynolds-number results were in agreement with experimental measurements on velocity distributions within the flow. At high Reynolds number, results were shown to converge to oscillatory flows that can be characterized by time-dependent clusters of large scale vortices. The dependence of the shedding frequency and growth rate of these structures on the geometry were investigated in [48]. The interactions between jet flow, recirculating flow and annulus flow, encountered in bluff-body flame burner, has been revealed in a vortex simulation [49].

The random vortex method was also applied to study reacting recirculating flows of premixed gases at high Reynolds numbers [50,51] utilizing the thin flame approximation [52] to model the combustion process. Results were used to study vorticity-flame-pressure interactions in a semiconfined, recirculation-stabilized premixed flame. Analysis of these results show how the volumetric expansion associated with burning can reduce the amplification of flow oscillation in recirculating flows when the pressure is kept constant, and how these oscillation can be amplified leading to large flame oscillation if the pressure field within the system is coupled with the flow processes [51,53]. These results address the problem of turbulent flame stabilization in a premixed stream and the associated combustor instabilities observed in such systems.

VIII. CLOSURE

Numerical simulation, using accurate schemes to integrate the unsteady equations governing reacting flow, can be applied to investigate important mechanisms of shear flow-combustion interaction in different systems and within a wide range of physical parameters. Mechanisms of flow combustion interaction are different in nonpremixed and premixed shear layers. Entrainment, associated with the formation of structures that develop due to natural shear flow instability, is the primary mechanism by which the flow enhances the rate of burning in both cases. Burning enhancement is substantial, especially at low Damkohler number where entrainment changes the reaction region from a thin front into a distributed zone. Strain may have some effect on the burning mechanisms especially at low Damkohler number where local extinction has been observed at regions of high strain rate in the nonpremixed shear layer. In the premixed shear layer, the reduction in the rate of burning due to strain is greater at high-Damkohler number.

Heat release establishes zones of density gradient within the vorticity layer. Baroclinic vorticity, generated from the interaction between these density gradients and material acceleration, reduces the growth rate of the instability in the nonpremixed case while enhancing it in the premixed case. The latter occurs even in the nonreacting case. Volumetric expansion, however, suppresses the instability in both cases. The effect is more pronounced at high-Damkohler number. Volumetric dilatation reduces the vorticity and weakens the large structures. Forcing at high amplitudes in the initial stages can be used to overcome this instability suppression.

Work is under way to extend the numerical methodology in different directions, e.g., (1) the formulation of a transport element method for confined flows in which the interaction between the interior flow and the

wall thermal boundary layer is important; (2) the application of the transport element method to flows in which pressure-density interaction plays a significant dynamic role [54]; (3) the implementation of fast solvers to reduce the computational effort from $O(N^2)$ to $O(N)$ [55]; (4) the implementation of a methodology to allow the application of the scheme to extended, multistep chemical kinetic models; and (5) the formulation of Lagrangian schemes for multiphase flow such as fuel droplets in gas streams.

REFERENCES

1. Clark, R.A., Compressible Lagrangian hydrodynamics without Lagrangian cells, in Numerical Methods for Fluid Dynamics II, ed by K.W. Morton and M.J. Baines, Clarendon Press, Oxford, 1986, pp. 255-272.
2. Fritts, M.J. and Boris, J.P., The Lagrangian solution of transient problems in hydrodynamics using triangular mesh, J. Comput Phys., 31, (1979) pp. 173-215.
3. Zabusky, N.J., Overman, II E.D., Regularization of contour dynamical algorithms. 1. tangential regularization, J. Comput. Phys., 52, (1983) pp. 351-373.
4. Chorin, A.J. and Bernard, P., Discretization of a vortex sheet with an example of roll-up, J. Comput. Phys., 13, 1973, pp. 423-428.
5. Leonard, A., Vortex methods for flow simulation, J. Comput. Phys., 37, 1980, pp. 289-335.
6. Ghoniem, A.F., Heidarinejad, G. and Krishnan, A. Numerical simulation of a thermally-stratified shear layer using the vortex element method, J. Comput. Phys., 79, 1988, pp. 135-166.
7. Ghoniem, A.F., Heidarinejad, G. and Krishnan, A., Turbulence-combustion interactions in a reacting shear layer, in Turbulent Reactive Flows, ed by Borghi and Murthy, Lecture Note in Engineering, 40, Springer-Verlag, New York, pp. 638-671 (1989).
8. Chorin, A.J., Hughes, T.J.R., McCracken, M.F. and Marsden, J.E., Product formulas and numerical algorithms, Comm. Pure App. Math., 31, (1978) pp. 205-256.
9. Hald, O., Convergence of vortex methods fro Euler's equations, SIAM J. Num. Anal., 16, 1979, pp. 726-755.
10. Beale, J.T. and Majda, A., Higher order vortex methods with explicit velocity kernels, J. Comput. Phys., 58, 1985, pp. 188-209.
11. Anderson, C. and Greengard, C., On vortex methods, SIAM. J. Numer. Anal., 22, 1985, pp. 413-440.
12. Ghoniem, A.F., Heidarinejad, G. and Krishnan, A., On mixing, baroclinicity and the effect of strain in a chemically reacting shear layer, the AIAA 26th Aerospace Sciences Meeting, January 11-14, Reno, Nevada, AIAA-88-0729.
13. Ghoniem A.F., and Ng K.K., Numerical study of a forced shear layer, Phy. Fluids, 30, 1987, pp. 706-721.
14. Krishnan, A., and Ghoniem, A.F., Numerical simulation of the structure of a heated jet in a cold environment, AIAA-89-0485, 27th Aerospace Sciences Meeting, Jan. 9-17, 1989/Reno, NV.

15. Chorin, A.J., Vortex models and boundary layer instability, SIAM J. Sci Stat. Comput., 1, 1980, pp. 1-21.
16. Leonard, A., Computing three dimensional incompressible flows with vortex elements, Ann. Rev. Fluid Mech., 15, 1985, pp. 532-559.
17. Ghoniem, A.F., Aly, H.M. and Knio, O.M., Three dimensional vortex simulations with application to axisymmetric shear layers, AIAA-87-0379, 25th AIAA Aerospace Sciences Meeting, Jan. 1987/Reno NV.
18. Cattolica, R.J. "Combustion-torch ignition: fuorescence imaging of NO_2 ," the 21st Symposium (International) on Combustion, the Combustion Institute, Pittsburg, PA, 1986, pp. 1551-1559.
19. Gutmark, E, Parr, T.P., Parr, D.M. and Schadow, K.C., Evolution of vortical structures in flames, 22nd Symposium (International) on Combustion, the Combustion Institute , Pittsburg, PA, 1988, pp. 523-529.
20. Saffman, P.G., The velocity of viscous vortex rings, Stud. App. Math., 49, 1970, pp. 371-380.
21. Knio, O.M. and Ghoniem, A.F.. Numerical study of a three-dimensional vortex method, J. Comput. Phys., in press, 1990.
22. Widnall, S.E., and Tsai, C-Y., The instability of the thin vortex ring of constant vorticity, Proc. Roy. Soc. Lond, Series A, 287, (1977) pp. 273-305.
23. Maxworthy, T., Some experimental studies on vortex rings, J. Fluid Mech., 81, 1977, pp. 465-495.
24. Knio, O.M., and Ghoniem, A.F., Three dimensional vortex simulation of entrainment augmentation due to streamwise structures, AIAA-89-0574, 27th Aerospace Sciences Meeting, Jan. 1989/Reno, NV.
25. Ashurst, W.T. and Meigburg, E., Three dimensional shear layers via vortex dynamics, J. Fluid Mech., 189, 1988, pp. 87-116.
26. Knio, O.M., and Ghoniem, A.F., Three dimensional vortex simulation of the rollup and entrainment in a shear layer, J. Comput. Phys., in press, 1990.
27. Krishnan, A., Vorticity-Combustion Interaction in Reacting Shear Flow, Sc.D. thesis, Department of Mechanical Engineering, M.I.T., 1989.
28. Raviart, P.A., Particle numerical models in Fluid Dynamics, in Numerical Methods for Fluid Dynamics II, ed by K.W. Morton and M.J. Baines, Claredon Press, Oxford, 1986, pp. 231-254.
29. Masutani, S.M., and Bowman, C.T., The structure of a chemically reacting plane mixing layer, J. Fluid Mech., 172, (1986) pp. 93-126.
30. Knio, O.M., Three Dimensional Lagrangian Simulation of Reacting Shear Flow, Ph.D. Thesis, Department of Mechanical Engineering, M.I.T., 1990.

31. Krishnan, A. and Ghoniem, A.F., Rollup and mixing in Rayleigh-Taylor flow," submitted for publication, J. Comput Phys., 1989.
32. Ghoniem, A.F., and Krishnan, A., Mixing patterns and the generation of vorticity in a density-stratified shear layer, Lecture Note in Engineering, Springer-Verlag, Proceedings of the Workshop on Physics of Compressible Turbulent Mixing, Princeton University, October 24-27, 1988, in press.
33. Ghoniem, A.F., and Krishnan, A., Baroclinic effects in stratified flows, submitted for publication, 1989.
34. Keller, J. and Daily, J.W., The effect of highly exothermic chemical reaction on a two-dimensional mixing layer, AIAA Journal, 23, (1985) pp. 1937-1945.
35. Krishnan, A. and Ghoniem, A.F., Origin and manifestation of flow-combustion interaction in a premixed shear layer, Proceedings of the 22nd Symposium (International) on Combustion, The Combustion Institute, Pittsburgh, PA, pp. 665-675 (1988).
36. Dimotakis, P.E., Two dimensional shear layer entrainment, AIAA Journal, 24 (1986) pp. 1791-1796.
37. Hiedarinejad, G. and Ghoniem, A.F., Vortex simulation of the reacting shear layer; effect of Reynolds number and Damkohler number, 27th Aerospace Sciences Meeting, Reno, NV, AIAA-89-0573.
38. Majda, A. and Sethian, J.A., The derivation and numerical solution of zero Mach number combustion, Combust. Sci. Tech., 42, 1985, p. 185.
39. Hiedarinejad, G., Numerical Simulation of the Reacting Shear Layer Using the Transport Element Method, Ph.D. Thesis, Department of Mechanical Engineering, M.I.T., 1989.
40. Ghoniem, A.F., and Heidarinejad, G., Effect of Damkohler number on the reactive zone structure in a shear layer, Combust. Flame, in press, 1990.
41. Knio, O.M. and Ghoniem, A.F., Three-dimensional Lagrangian simulation of a reacting shear layer, AIAA-90-0150, 28th AIAA Aerospace Sciences Meeting, Jan 1990/Reno, NV.
42. Krishnan, A. and Ghoniem, A.F., Vorticity-combustion interactions in a reacting jet, 12th International Colloquium on the Dynamics of Explosion and reacting Systems, July 1988, Proceedings to appear.
43. Riley, J.J. and McMurtry, P.A., the use of direct numerical simulation in the study of turbulent, chemically reacting flows, in Turbulent Reactive Flows, ed by Borghi and Murthy, Lecture Note in Engineering, 40, Springer-Verlag, New York, pp. 486-514 (1989).
44. Chorin, A.J., Numerical study of slightly viscous flow, J. Fluid Mech., 57, 1973, 785-7794.

45. Chorin, A.J., Vortex sheet approximation of boundary layers, J. Comput. Phys., 27, 1987, pp. 423-442.
46. Ghoniem, A.F. and Gagnon, Y., Vortex simulation of laminar recirculating flow, J. Comput. Phys., 68, 1987, pp. 346-377.
47. Sethian, J.A. and Ghoniem, A.F., Validation study of vortex methods, J. Comput. Phys., 74, 1988, pp. 283-317.
48. Najm, H. and Ghoniem, A.F., Numerical simulation of the convective instability in a dump, AIAA/SAE/ASME/ASEE 23rd Joint Propulsion Conference, San Diego, CA, 1987, AIAA-87-1874, to appear in AIAA J.
49. Martins, L.F., Ph.D. thesis, Department of Mechanical Engineering, M.I.T. 1990.
50. Ghoniem, A.F., Chorin, A.J. and Oppenheim, A.K., Numerical modelling of turbulent flow in a combustion tunnel, Phil. Trans. R. Soc. Lond., A304, (1982) pp. 303-325.
51. Ghoniem, A.F., and Najm, H., Numerical simulation of the coupling between the vorticity and pressure oscillations in combustor instability, AIAA/SAE/ASME/ASEE 25th Joint Propulsion Conference, Monterey, CA, AIAA-89-2665.
52. Ghoniem, A.F. and Knio, O.M., Numerical simulation of flame propagation in constant volume chambers, Proceedings of the 21st Symposium (International) on Combustion, the Combustion Institute, Pittsburgh, PA. (1986) pp. 1313-1320.
53. Ghoniem, A.F. and Najm, H., Numerical simulation of the coupling between the vorticity and pressure oscillation in combustion instability, AIAA/ASME/SAE/ASEE 25th Joint Propulsion Conference, Monterey, CA/July 1989, AIAA-89-2665.
54. Ghoniem, A.F., Vortex methods in two and three dimensions, a review and some extensions, Proceedings of the First AIAA/ASME/SIAM/APS National Fluid Dynamics Congress, Cincinnati, OH, July 1988, p. 658.
55. Ambrosiano, J., Greengard, L. and Rockhin, V., The Fast Multipole Method for Gridless Particle Simulations, Research Report YALEU/DCS/RR-565, Sep. 1987, Yale University.

FIGURE CAPTIONS

Figure 1. The rollup of an incompressible, uniform density, nonreacting, temporally-growing shear layer in which the top and bottom streams move at the same speed but in opposite directions and the initial vorticity distribution is gaussian. The initial amplitude of the sinewave perturbation is 1% of its wavelength, which is taken as the most unstable wavelength for this flow. The results are shown in terms of (a) the vortex elements and their velocity vectors; and (b) the isoscalar lines ($s = 0$ in the top stream and $s = 1$ in the bottom stream with an error function distribution in between).

Figure 2. The development of an incompressible, nonreacting, spatially developing shear layer between a fast, top stream and a slow, bottom stream. The velocity ratio across the layer is 2 and the vorticity distribution at the left-hand side of the domain, where the splitter plate ends, is gaussian. The figures show all the vortex elements used in the computation and their velocity vector (measured with respect to the mean velocity of the flow). The confining walls are slip boundaries. Three cases are shown: (a) the layer is unforced. (b) the layer is forced at the most unstable wavelength and the amplitude of the perturbation is 1% of the wavelength. (c) The layer is forced at the most unstable wavelength and its first subharmonic, and the two amplitudes are equal to 1% of the fundamental wavelength.

Figure 3. (a) Time-average streamwise velocity profiles for the case shown in figure 2a, computed at sections $x = 3, 3.5, 4, 4.5$ and 5. x is measured from the left-hand side of the domain, $x = x_0$, and is normalized with respect to the channel height, while $y_0 = 0$. U_h and U_l are the high and low speed stream velocities. Computational results are shown in solid lines and experimental measurements of Masutani and Bowman [29] are shown in open symbols.

(b) Time-average streamwise velocity fluctuations for the same case as in (a), computed at the same sections and plotted against experimental measurements from the same reference.

Figure 4. The deformation of a thin vortex ring, represented computationally by a single vortex filament, when excited at an unstable wavenumber (number of waves around the ring) of six. The radius of the ring core is 0.25 of the radius of the ring. The plots are obtained by projecting the ring on two planes normal (on the left-hand side) and parallel (on the right-hand side) to the direction of propagation of the ring under its own self-induced velocity.

Figure 5. The wavenumber of the most unstable mode, n^* , of a vortex ring plotted against its normalized self-induced velocity, $V = 4\pi RV/\Gamma$ where R and Γ are the radius and circulation of the ring, respectively. The figure shows a comparison between the experimental results, \times ; the analytical results of the long wavelength instability, \circ ; the numerical results of the long wavelength instability, Δ ; the analytical results of the short wavelength instability, \square for constant vorticity distribution within the core and $+$ for quadratic vorticity distribution; and the computed results of the short wavelength instability, $\langle \rangle$ for coarse numerical discretization and $*$ for fine discretization.

Figure 6. Perspective views, taken from the point of view of an observer standing ahead of the ring and looking at an angle 60° with respect to the direction of propagation, of a vortex ring whose core radius is 0.275 of the ring radius. The ring is initially excited using 12 waves around. All the filaments used to discretize the ring are shown. The ring is propagating upwards.

Figure 7. Three-dimensional perspective views of the isoscalar surface $s = 0$, initially coinciding with an x - y plane located in the middle of the domain shown in the figure. The shear layer is periodic in two directions. At time $t = 0$, the layer is perturbed in the streamwise direction, x , at the most unstable wavelength, and in the spanwise direction, y , at one-half of this wavelength. The amplitudes of the perturbations are equal to 2% of the streamwise wavelength. The initial vorticity follows a gaussian distribution in the spanwise direction, z , as in the two-dimensional case.

Figure 8. (a) Streamwise vorticity; and (b) scalar distribution in the three-dimensional simulation of the periodic shear layer shown in figure 7. Contours are shown in a y - z plane which cuts through the core of the spanwise eddy at the middle of the domain of figure 7. Positive vorticity is indicated by broken lines while negative vorticity is depicted by continuous lines. For the scalar, $s > 0$ is shown in continuous lines and $s < 0$ is shown in broken lines, $-0.5 \leq s \leq 0.5$.

Figure 9. (a) Streamwise vorticity; and (b) scalar distribution in the three-dimensional simulation of a periodic shear layer shown in figure 7. Contours are shown in the y - z plane which cuts through the braids at a distance 15% of the wavelength into the domain from the left-hand side. See figure 8 for convention.

Figure 10. (a) Time-average scalar concentration for the flow in figure 2a, computed at $x = 5$ for a range of Peclet number, P_e . At $x = 0$, the concentration is $s = 0$ in the upper stream and $s = 1$ in the lower stream. Solid lines show the results of the computations and open symbols depict the experimental measurements of Masutani and Bowman [29].
(b) Time-average concentration fluctuations for the same flow as in (a).

Figure 11. The eddy size in the two, y ; and three, x ; dimensional computations of figures 1 and 7, respectively. The eddy size is defined by the cross-stream distance between the contours $s = 0.03$ and $s = 0.97$.

Figure 12. The rollup of an incompressible, nonuniform density, nonreacting, temporally-growing shear layer in which the top, heavy stream moves to the right and the bottom, light stream moves to the left at the same speed. The initial conditions are the same as in figure 1, except for the density distribution across the layer which is taken as an error function. $1 \leq \rho \leq 5$. The density ratio across the layer is five. The results are shown in terms of: (a) the isoscalar lines ($s = 0$ and in the top stream and $s = 1$ in the bottom stream); and (b) the vorticity contours. Broken lines indicate positive vorticity and solid lines indicate negative vorticity.

Figure 13. Three-dimensional perspective views of the isoscalar surface $s = 0$, initially coinciding with an x - y plane in the middle of the domain. The flow is incompressible but with variable density. Initially, the streamwise velocity and density vary only in the cross-stream, z -direction according to

similar error functions with different boundary conditions: $-1 \leq u \leq 1$ and $1 \leq p \leq 2$. The shear layer is periodic in the x and y directions. All other conditions are similar to the case presented in figure 7.

Figure 14. Results of a computation of a spatially-developing, reacting shear layer using an incompressible flow model and Arrhenius chemical kinetics. Figure 2a shows the vortex elements are their velocity vectors for this case (since the flow is incompressible, the reaction does not affect the dynamics). The figure shows contours of (a) the top stream reactant's concentration; (b) product concentration; (c) vorticity; and (d) temperature.

Figure 15. Results of a spatially-developing reacting shear layer using an incompressible flow model and temperature-independent kinetics. The dynamic field is the same as that shown in figure 2a. The figure shows (a) the product integral, $\int c_p dy$, across the layer for a reacting perturbed shear layer, similar that shown figures 2 and 14, and across an unperturbed shear layer where rollup is suppressed; (b) the product integral as a function of the Damkohler number; (c) The product integral as a function of the Reynolds number, the lines are computed for $R_e = 5000$ and 10000 while the points 1, 2, and 3 are computed at $R_e = 500$, 2500 and 50000 , respectively, D_{ax} is a Damkohler number based on the local value of x ; and (d) the total amount of product in the field, $\iint c_p dy dx$ as a function of the reactants ratio across the layer.

Figure 16. Results of a three-dimensional simulation of doubly periodic reacting shear layer between two reacting stream. The dynamics of this flow is the same as that in figure 7 since the flow is incompressible. The figure shows: (a) the product concentration (left) and reaction rate (right) on an x - z spanwise plane located at the middle of the domain in figure 7. (b) The product concentration (left) and reaction rate (right) across the section described in figure 8. (c) The product concentration (left) and reaction rate (right) across the section described in figure 9. Results are shown in gray scale in which the maximum value is indicated by black and the minimum value is shown in white. The gray scale for the product concentration is fixed, $0 \leq c_p \leq 1$, while the gray scale for the reaction rate is floating, $W_{min} \leq W \leq W_{max}$.

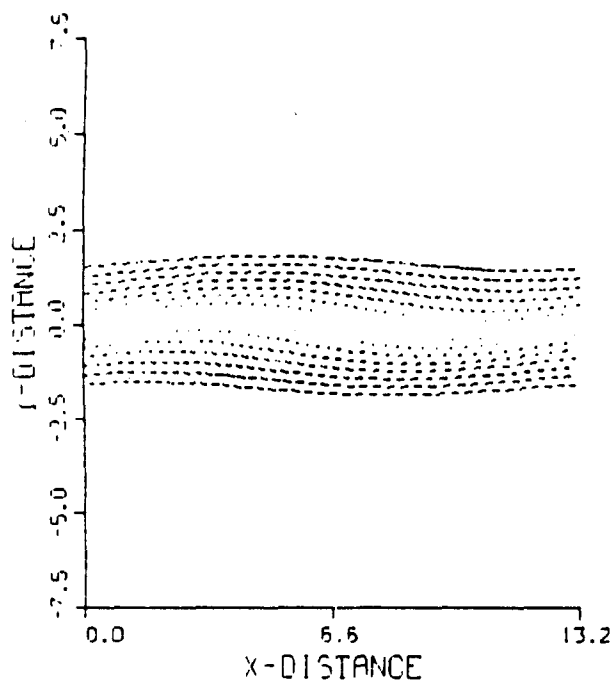
Figure 17. Product distribution within the initial stages in a reaction jet using a compressible flow model with Arrhenius chemical kinetics. The model is periodic in the streamwise direction. Results are shown at three time steps for: (a) $A_f = 150$; and (b) $A_f = 750$.

Figure 18. The distribution of the reaction rate within one side of the centerline of the reacting jet of figure 16, shown using a gray scale for (a) $A_f = 150$ and (b) $A_f = 750$. Results are shown in gray scale in which the maximum value is indicated by black and the minimum value is shown in white.

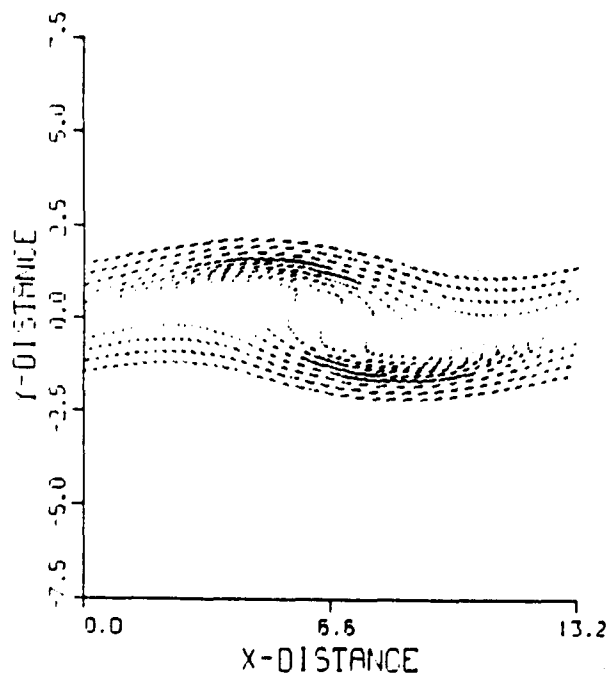
Figure 19. The roll-up of a compressible, temporally growing reacting shear layer between cold premixed reactants in the top stream and hot products in the bottom stream. Results are shown in terms of: (a) the reaction rate (shown in gray scale); and (b) the product concentration contours. The temperature ratio across the layer is five.

Figure 20. The total mass of products formed within the premixed reacting shear layer shown in figure 19, compared with the same quantity for a laminar flame propagating through the same mixture. Results are shown for three different values of A_f . Straight lines show the total mass of products formed in the corresponding laminar flame.

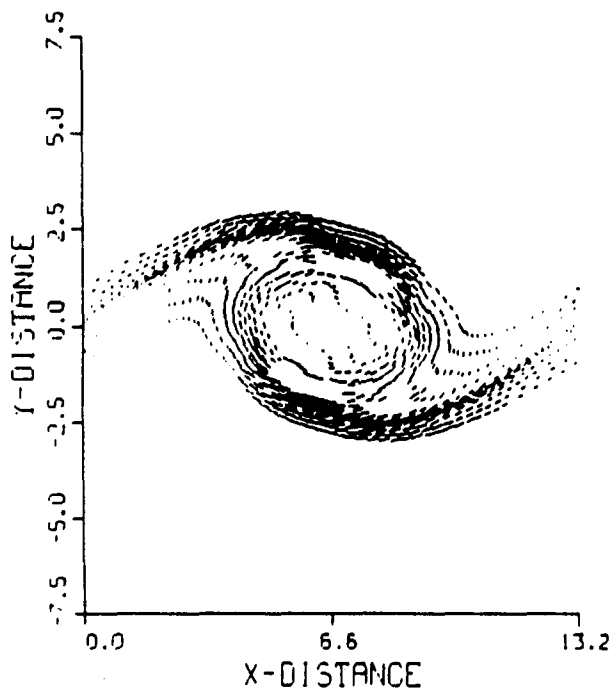
Figure 21. The total mass of products and the length of the line of maximum reaction rate in a premixed reacting shear layer similar to the one shown in figure 19, and in the corresponding laminar flame. The temperature ratio across the layer is three, $P_e = 200$ and $T_a = 5$.



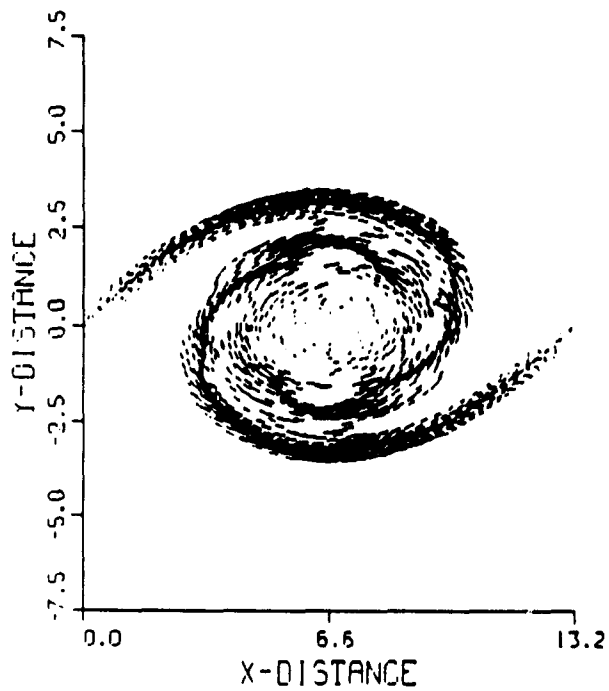
$t = 5.5$



$t = 11.0$

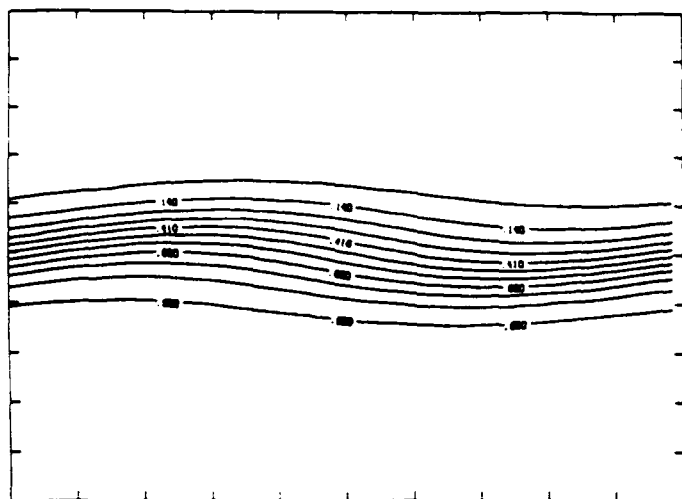
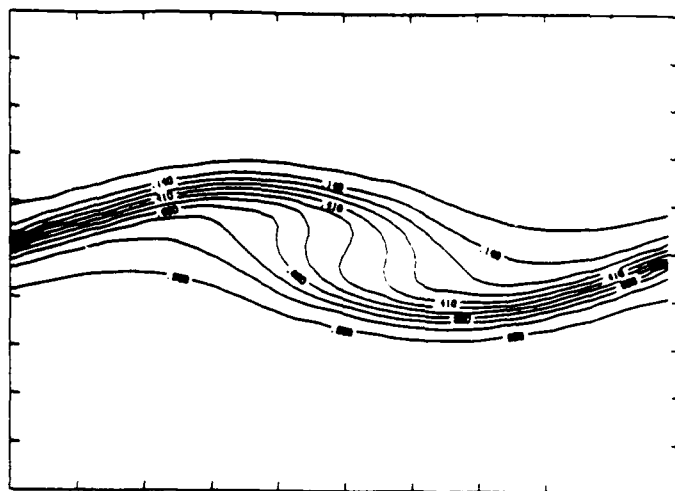


$t = 16.5$

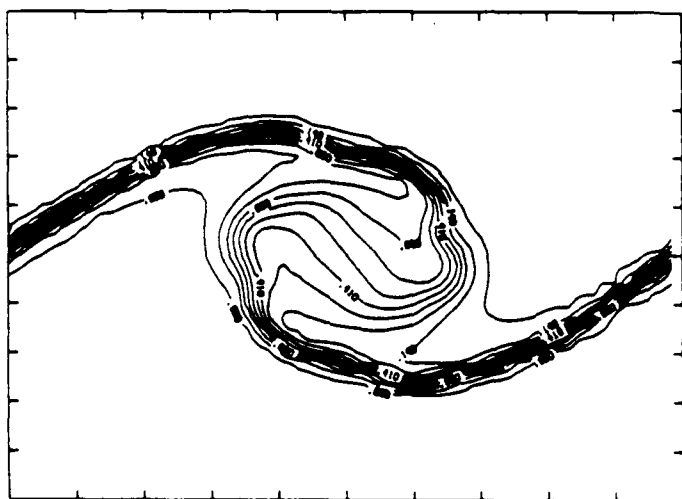


$t = 22.0$

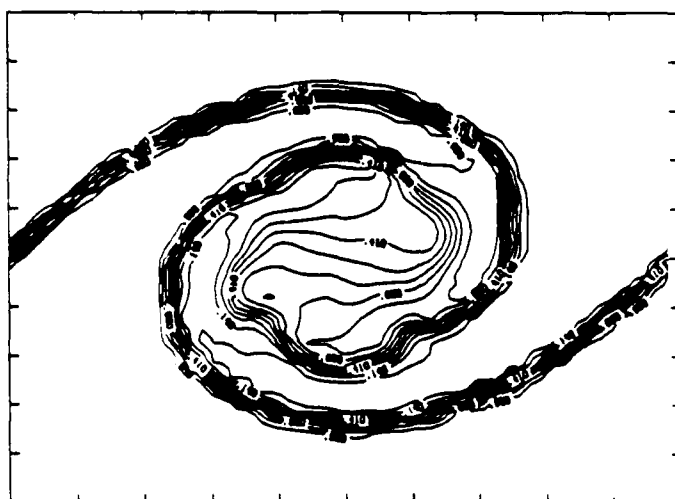
Figure 1a


$$t = 5.5$$


t = 11.0

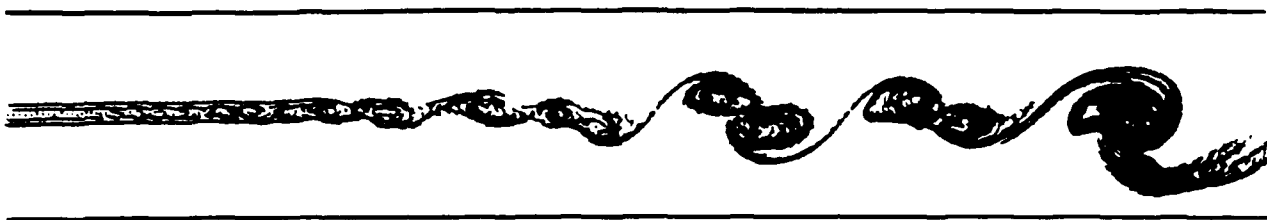


t = 16.5



t = 22.0

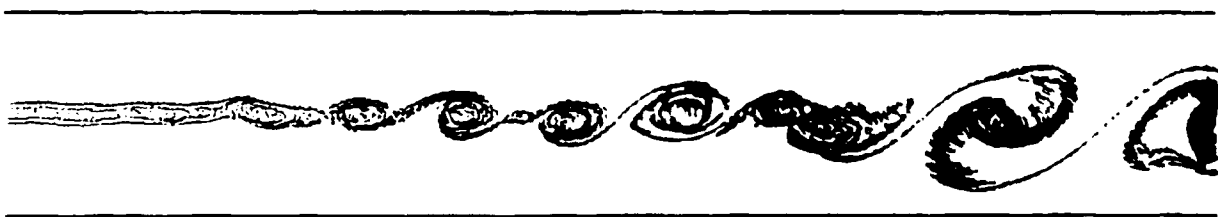
Figure 1b



(a)

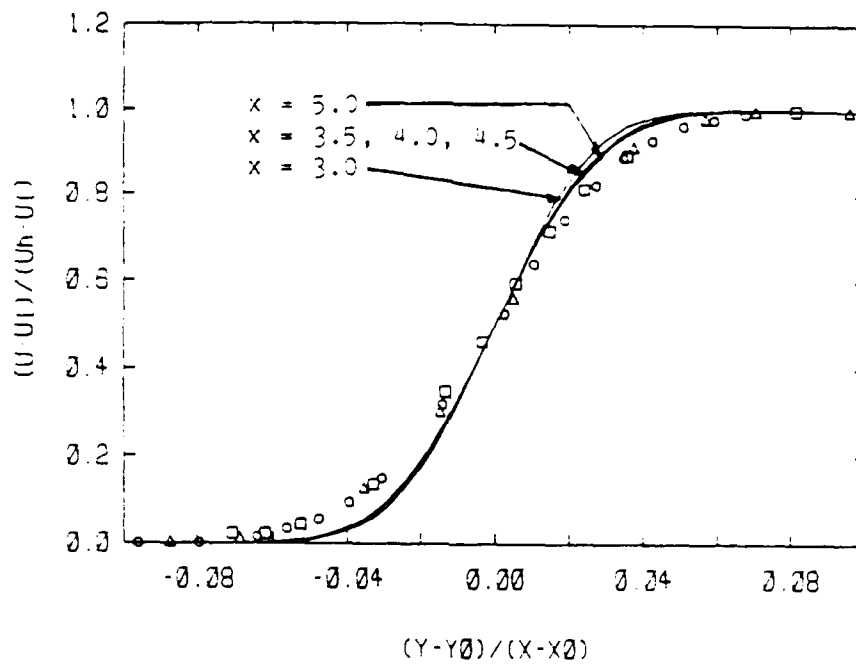


(b)

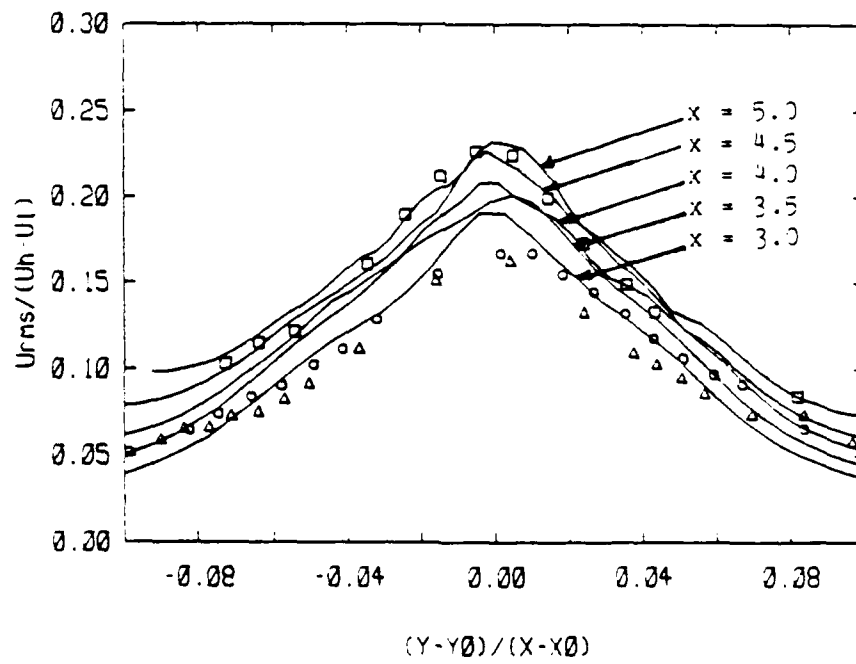


(c)

Figure 2



(a)



(b)

Figure 3

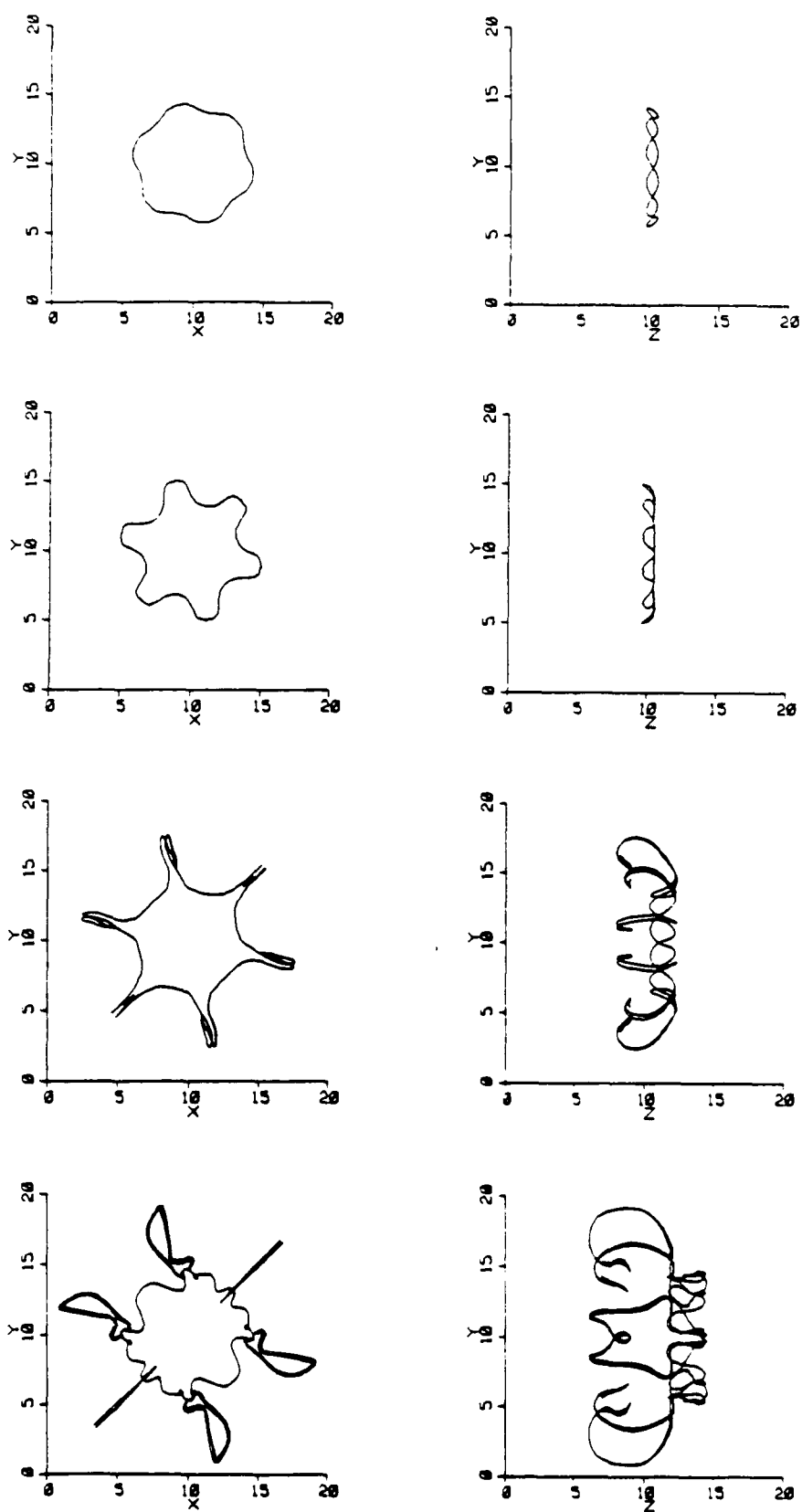


Figure 4

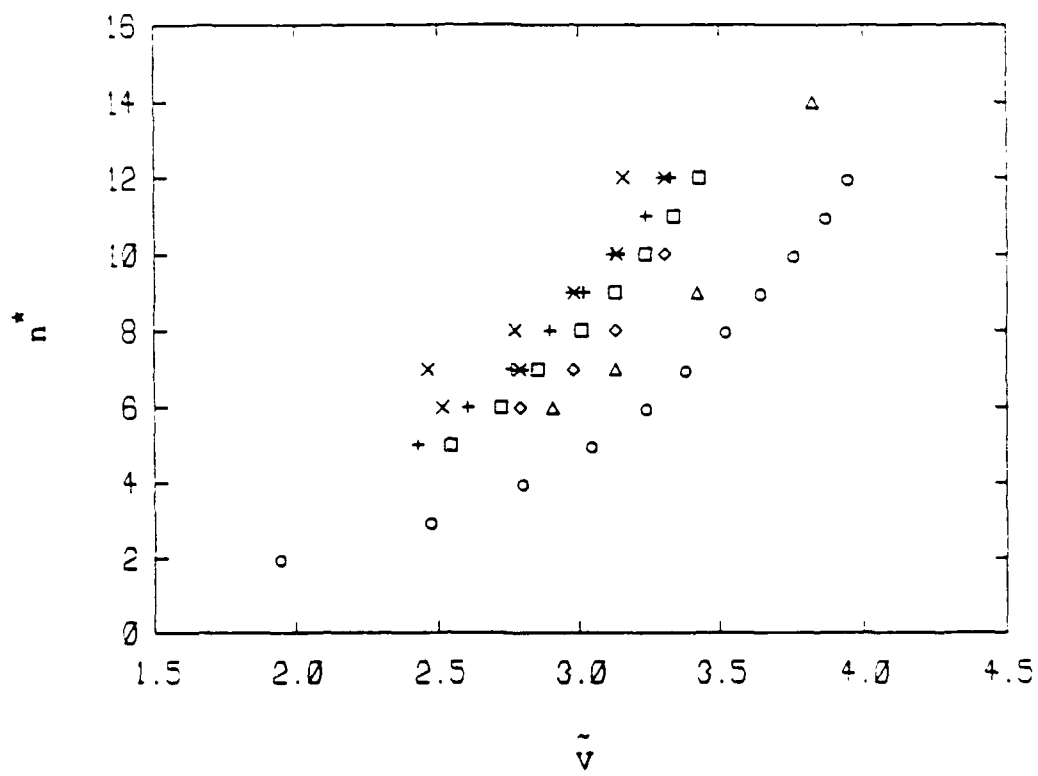


Figure 5

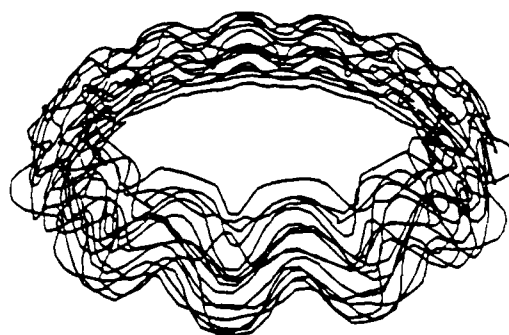
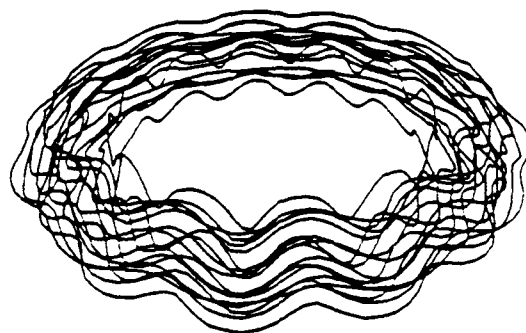
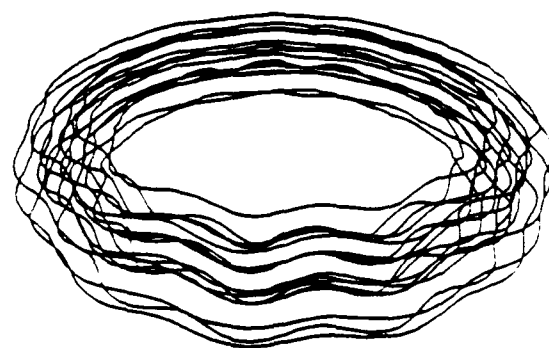
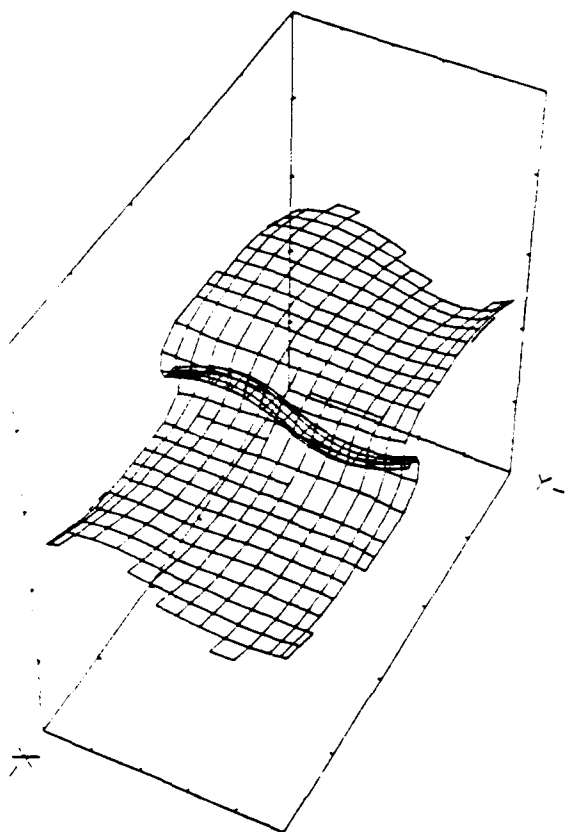
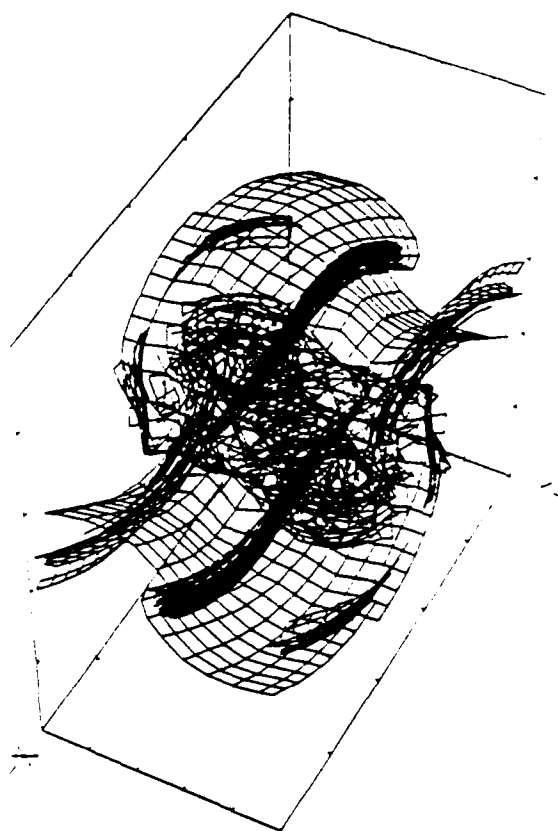


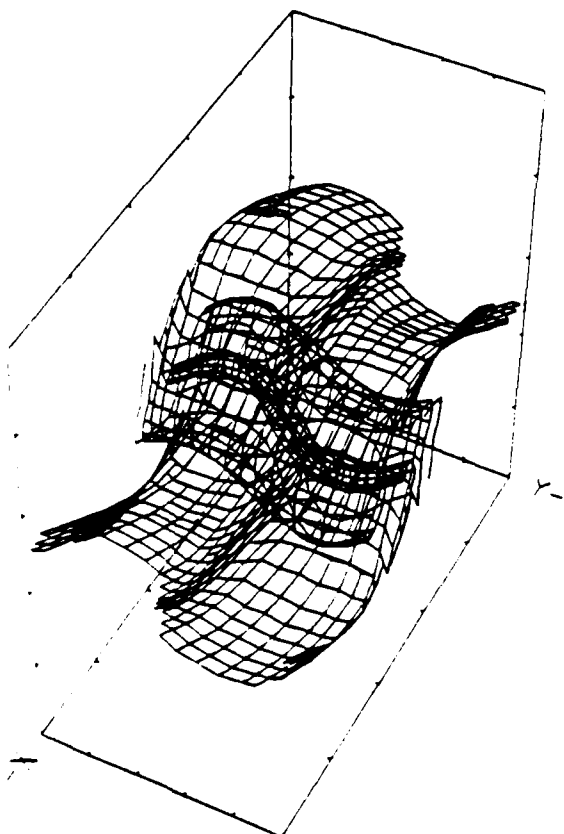
Figure 6



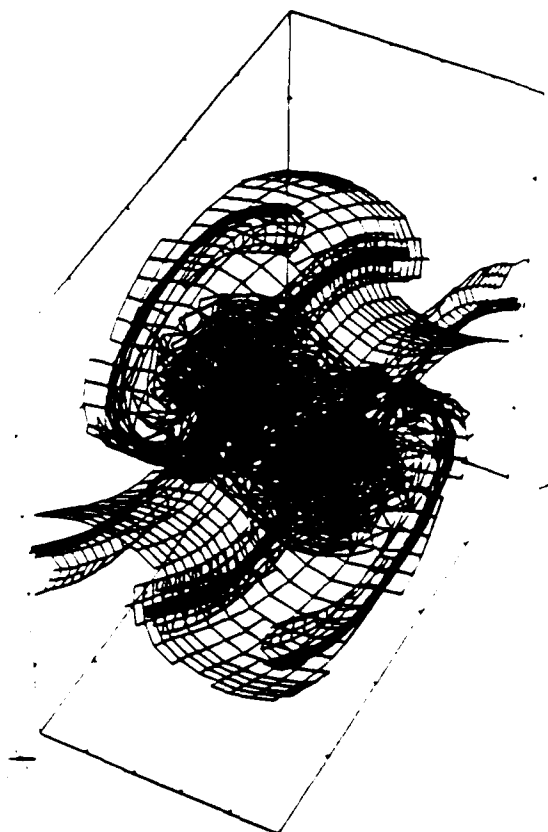
$t = 8.0$



$t = 16.0$



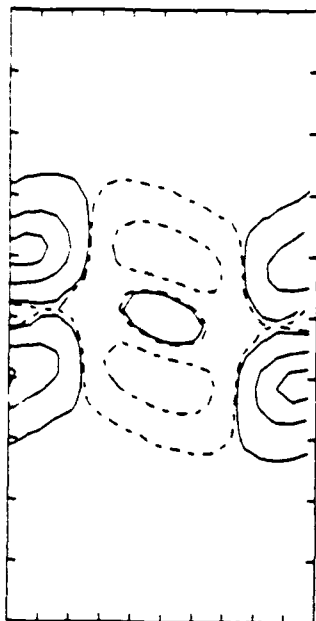
$t = 12.0$



$t = 18.0$

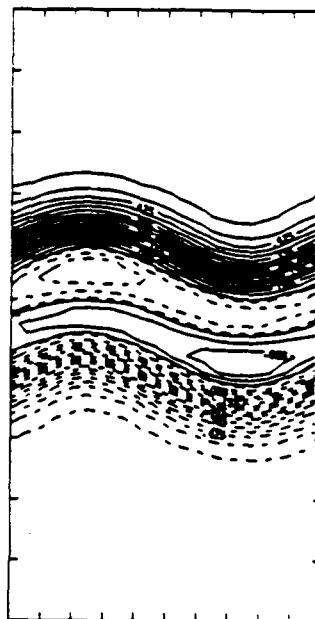
Figure 7

(a)

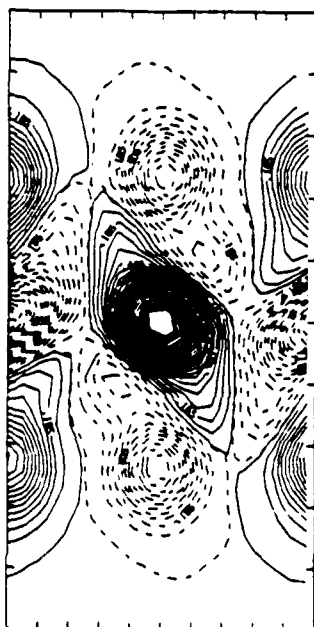


$t = 8.0$

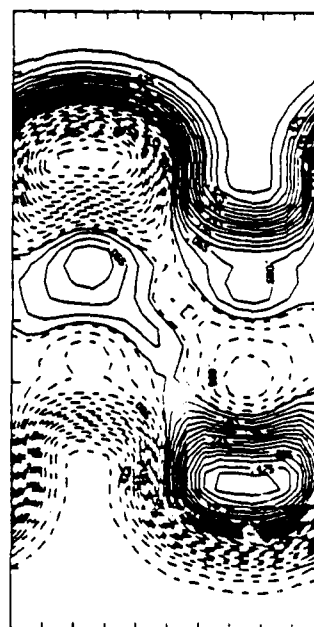
(b)



$t = 8.0$



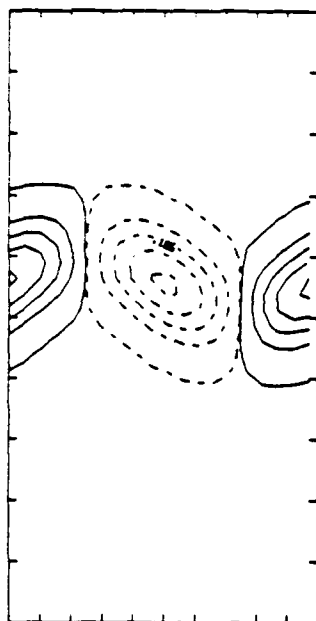
$t = 16.0$



$t = 16.0$

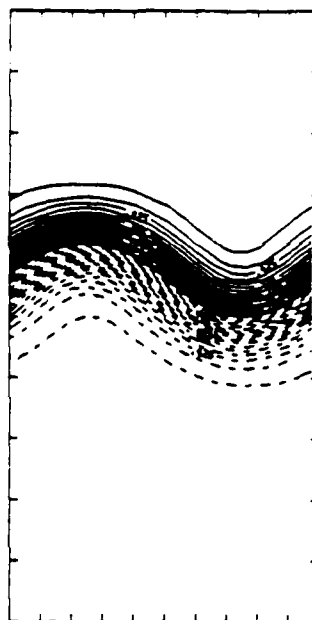
Figure 8

(a)

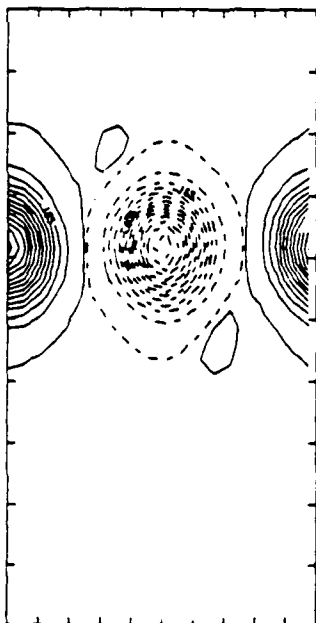


$t = 8.0$

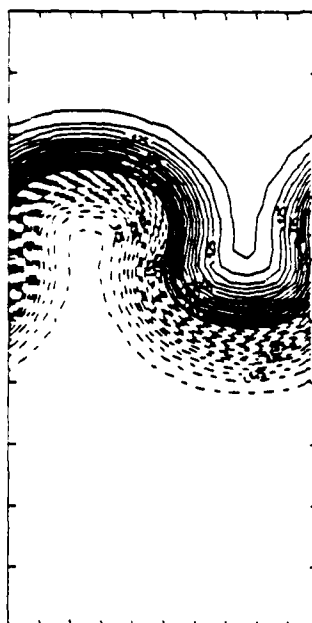
(b)



$t = 8.0$



$t = 16.0$



$t = 16.0$

Figure 9

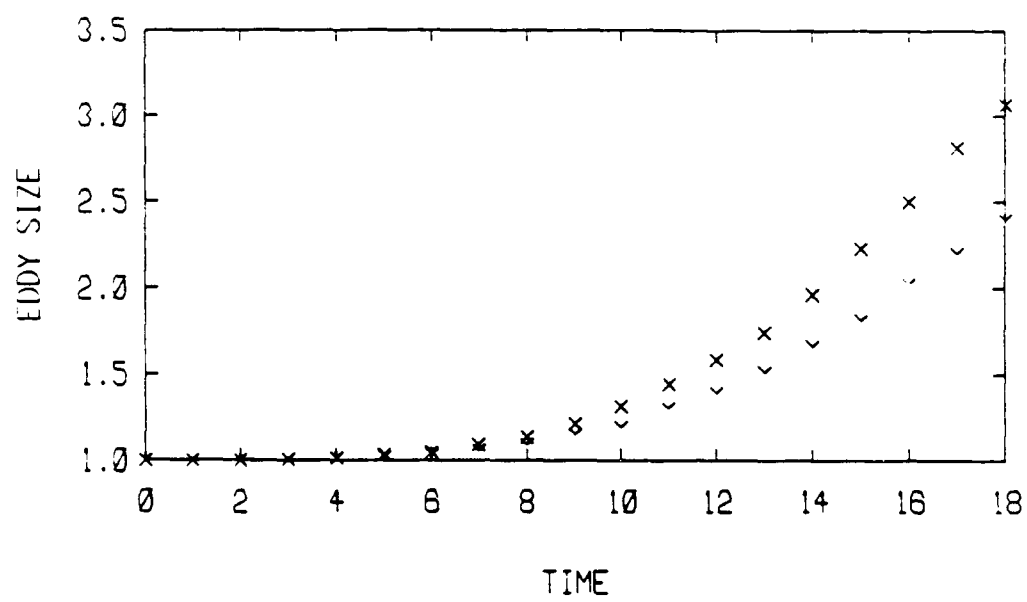
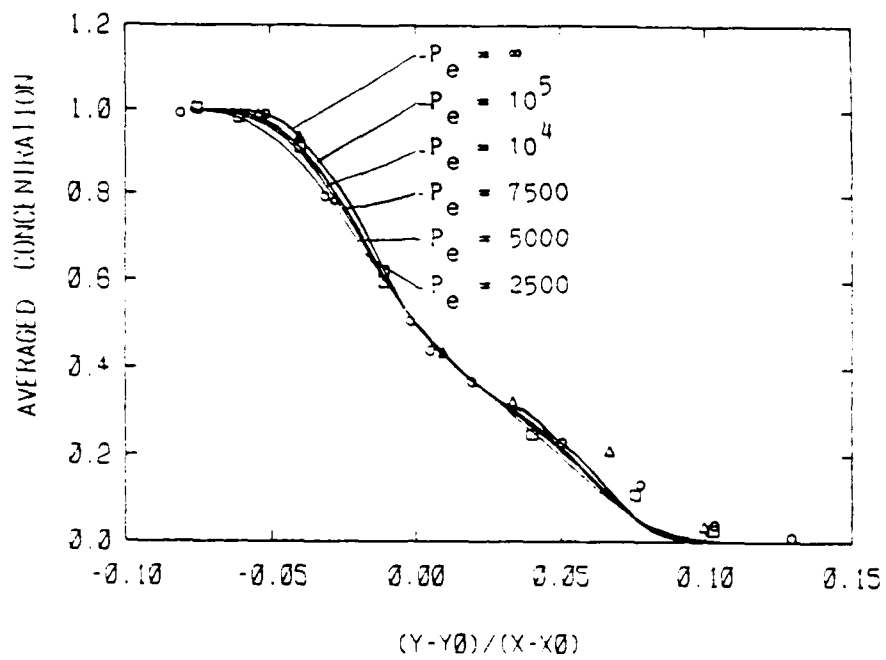
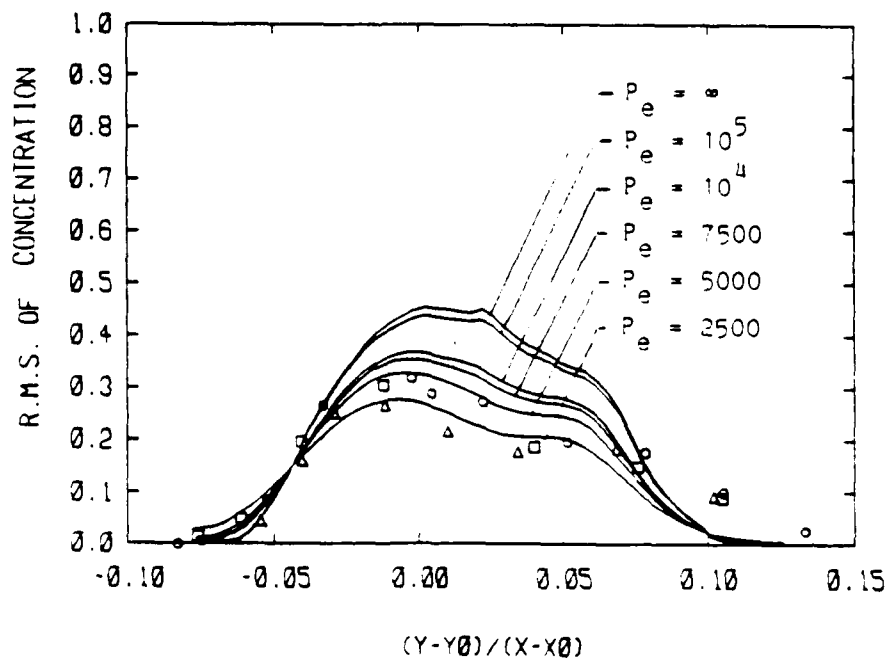


Figure 10

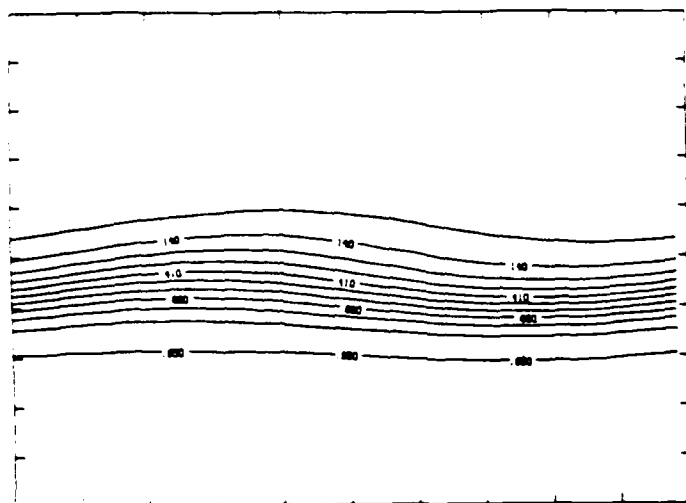


(a)

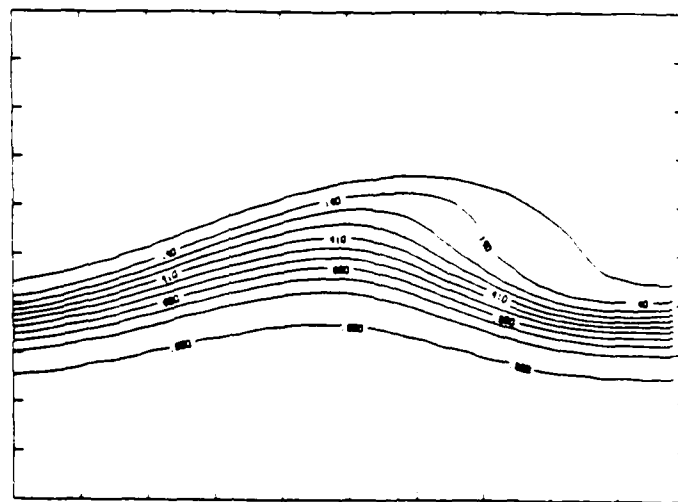


(b)

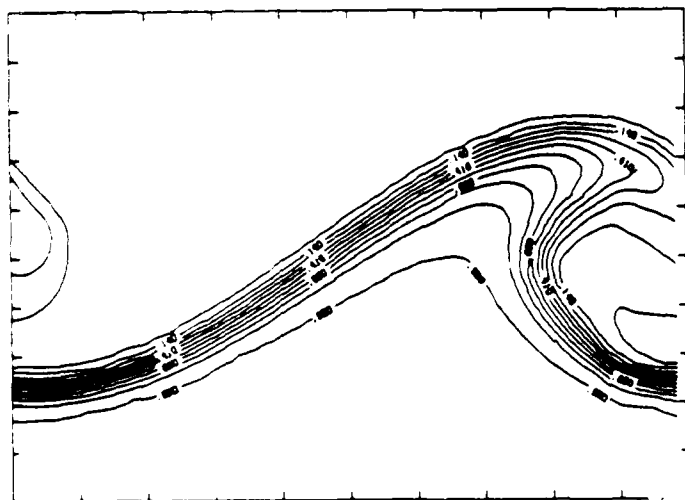
Figure 11



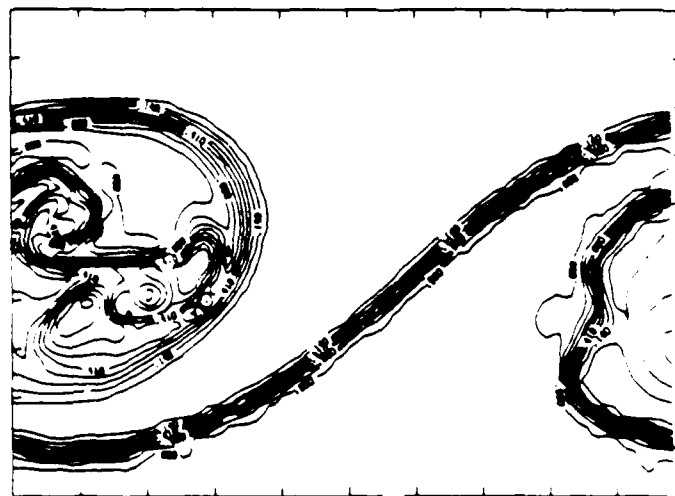
$t = 5.5$



$t = 11.0$

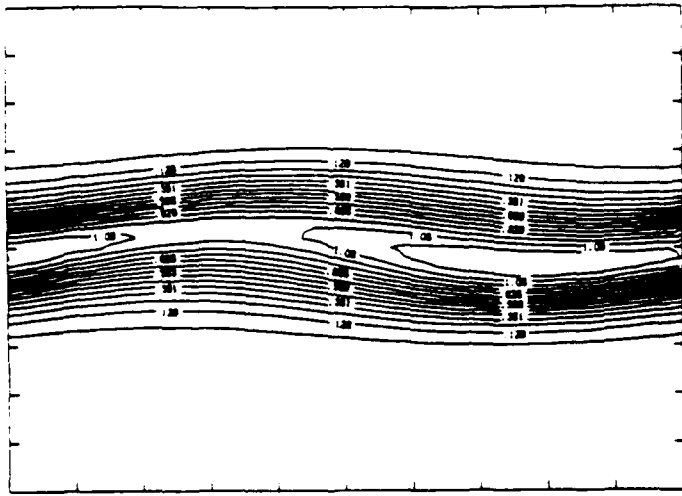


$t = 16.5$

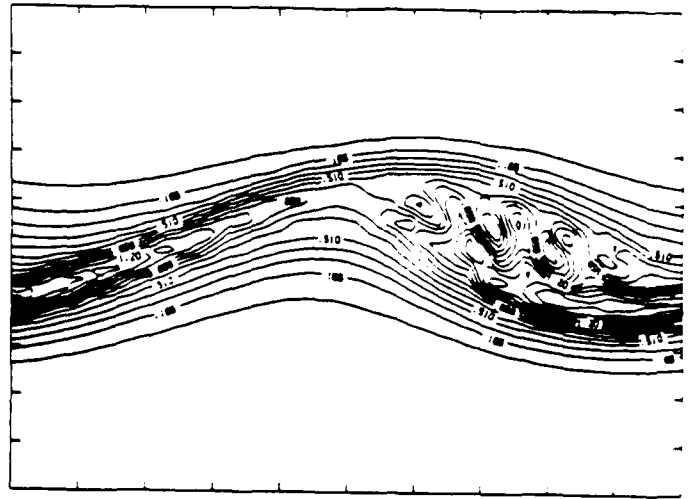


$t = 22.0$

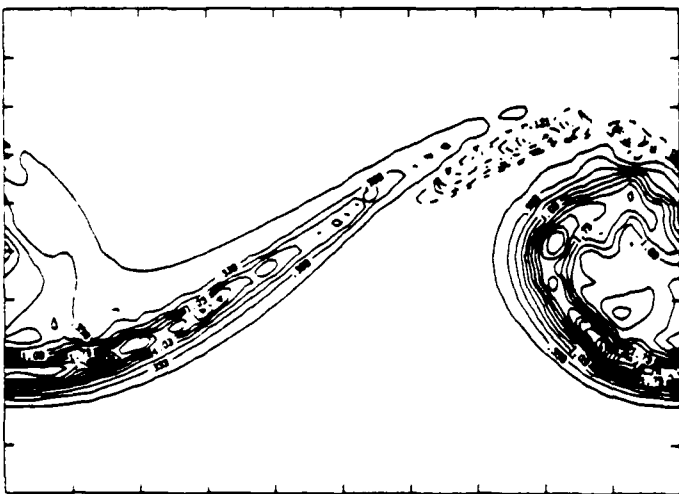
Figure 12a



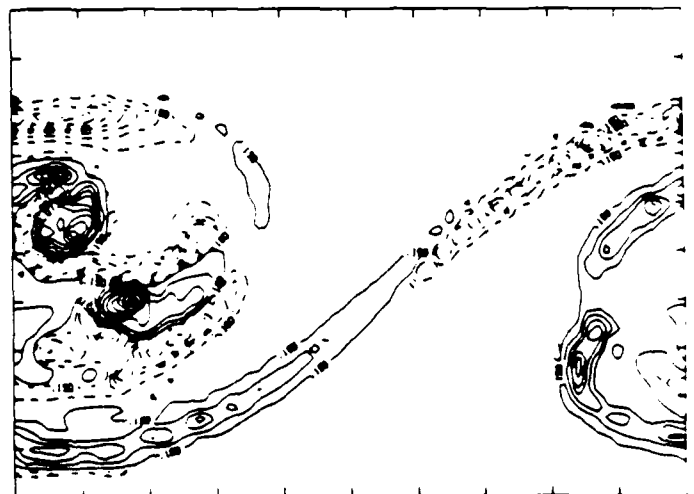
$t = 5.5$



$t = 11.0$

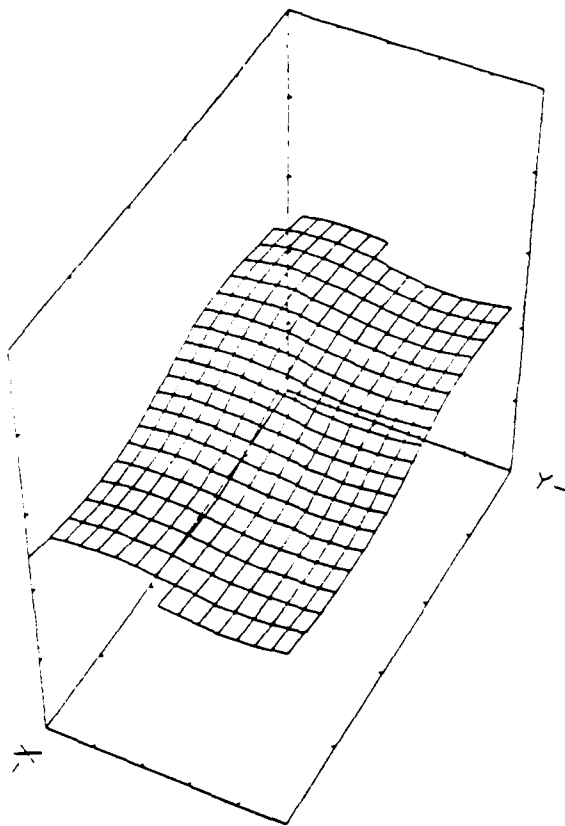


$t = 16.5$

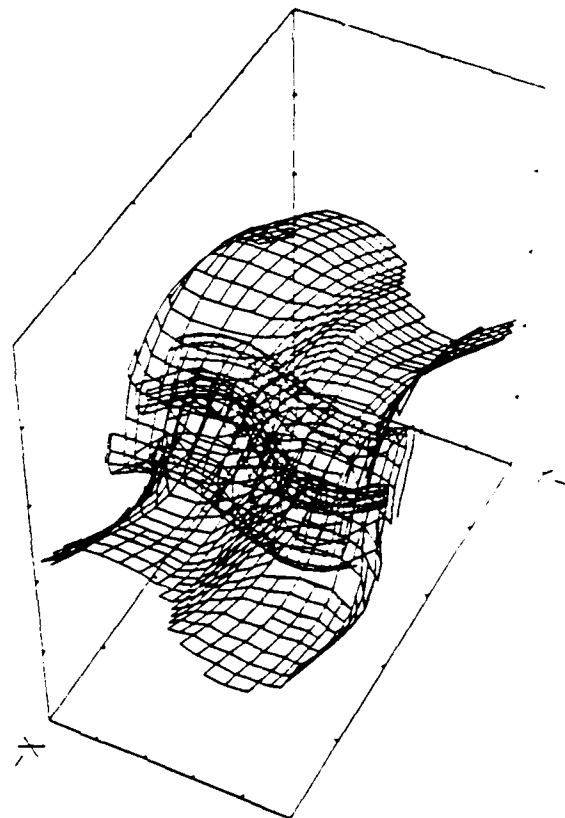


$t = 22.0$

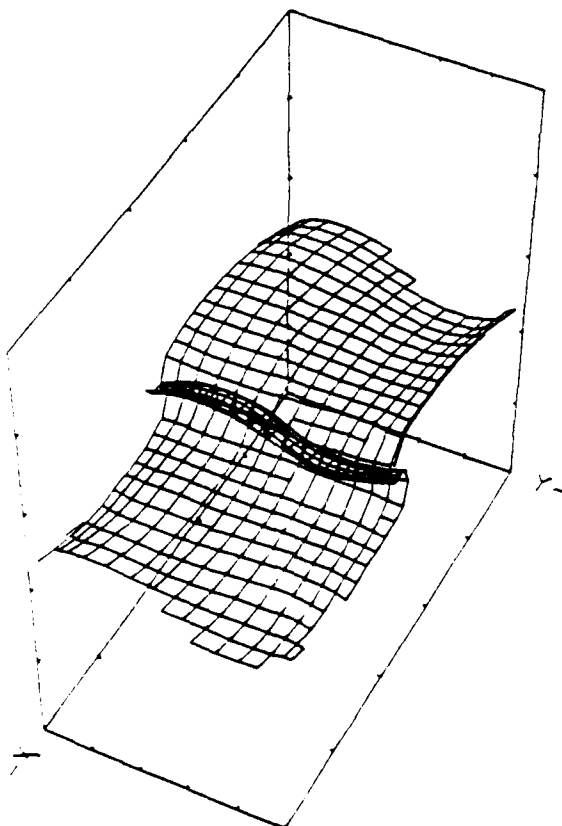
Figure 12b



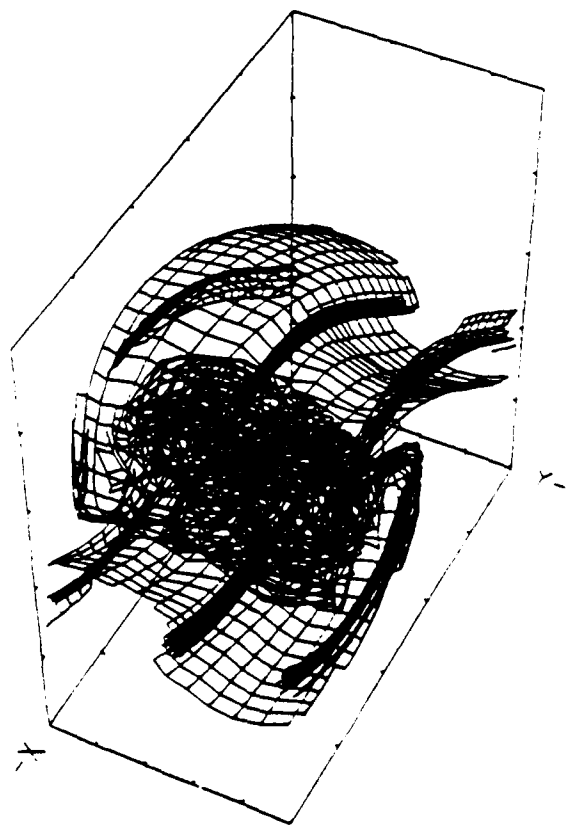
$t = 4.0$



$t = 12.0$

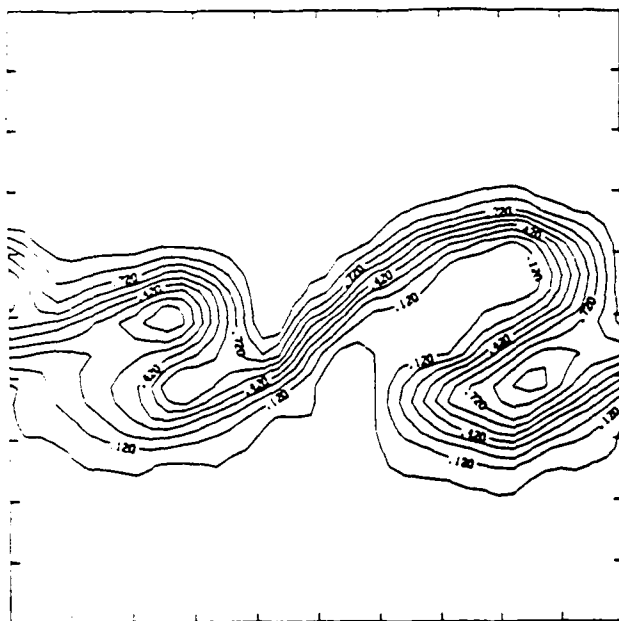


$t = 8.0$

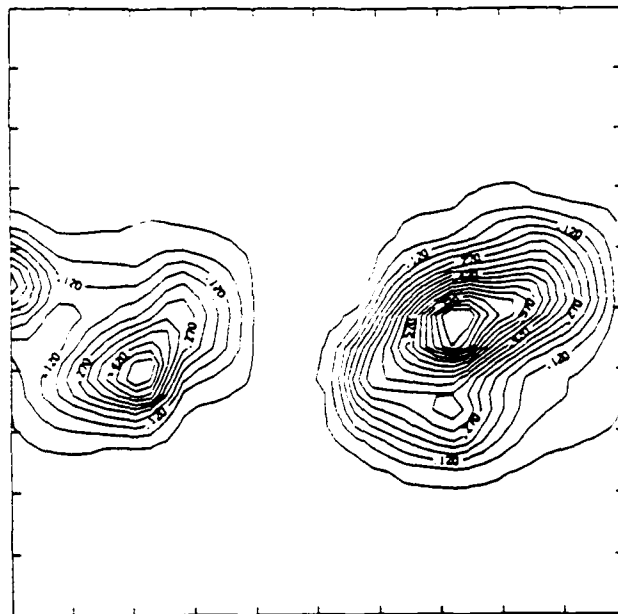


$t = 16.0$

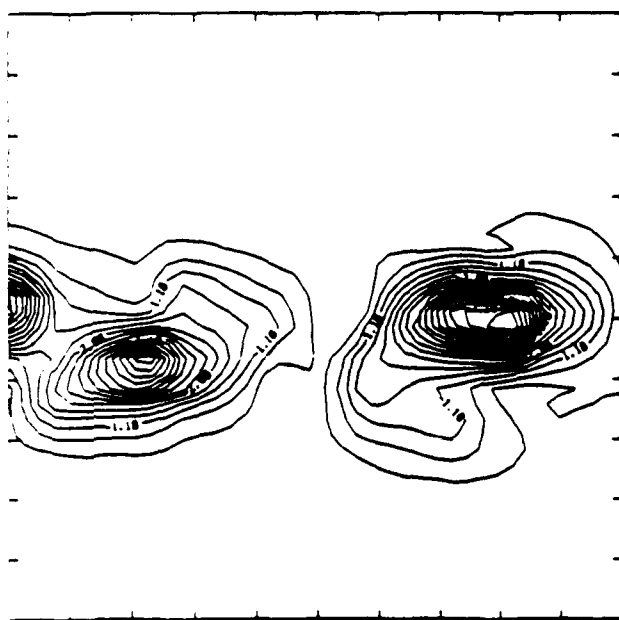
Figure 13



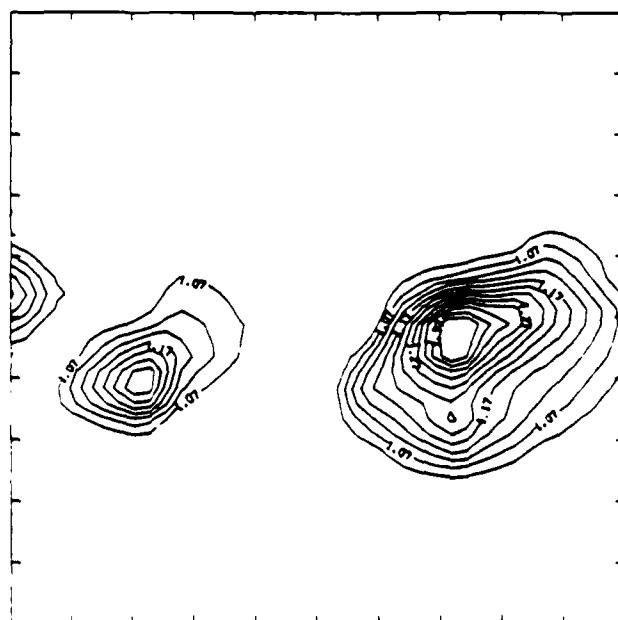
(a)



(b)

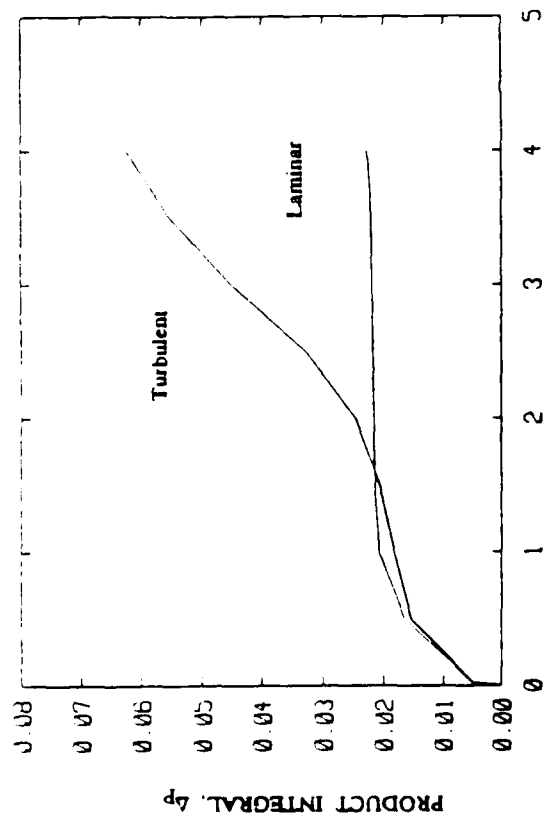


(c)



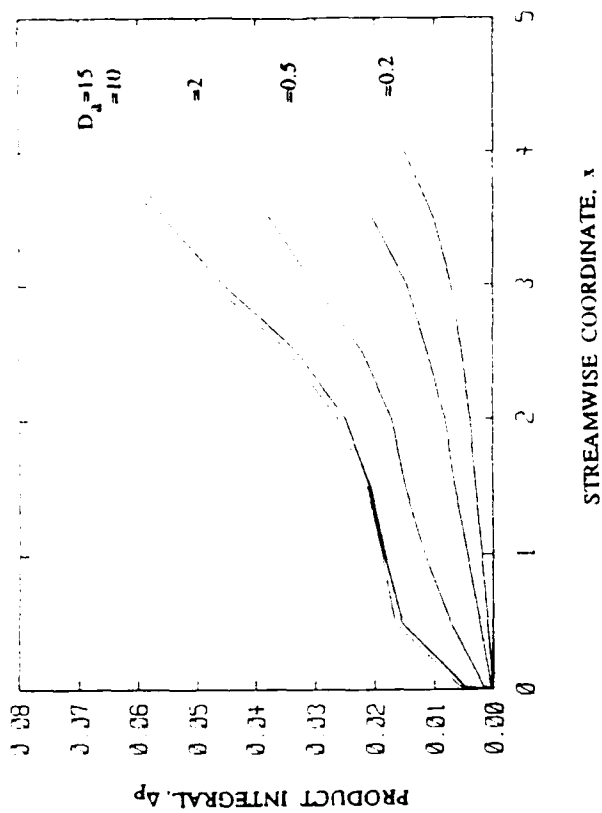
(d)

Figure 14



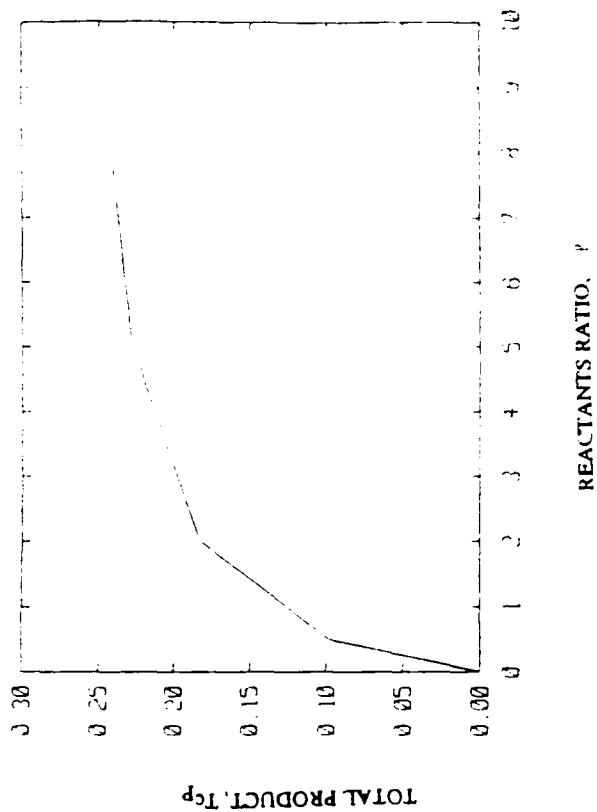
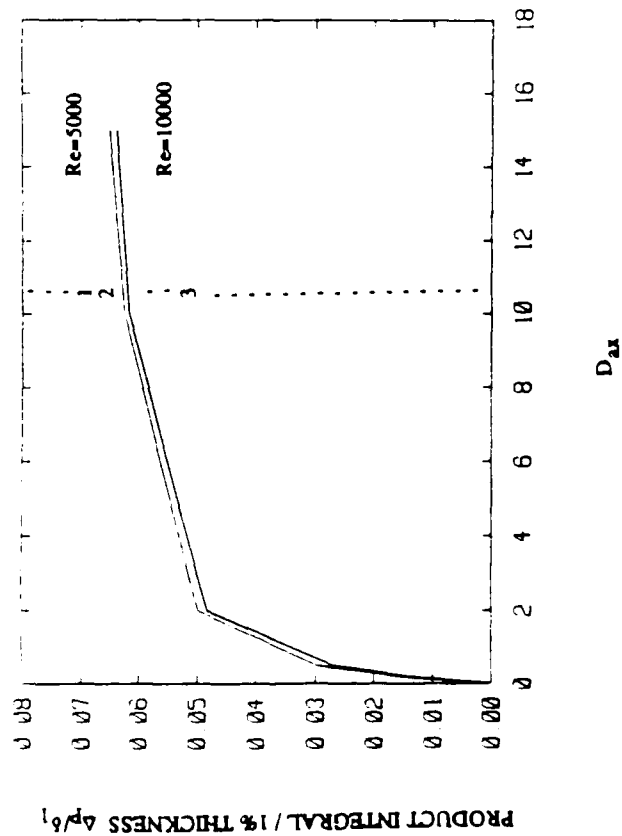
(a)

STREAMWISE COORDINATE, x



(b)

STREAMWISE COORDINATE, x



(d)

Figure 15

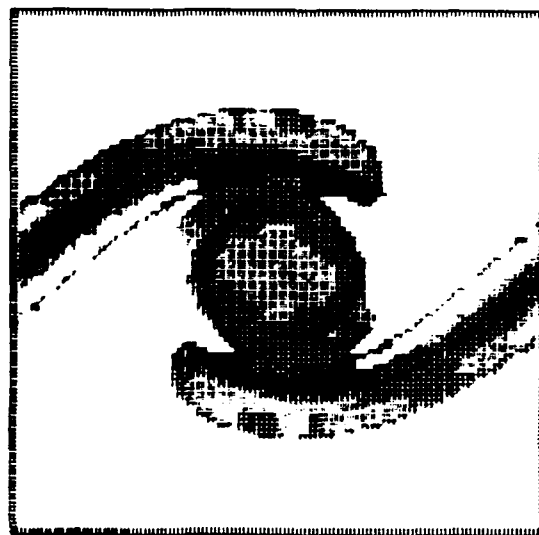
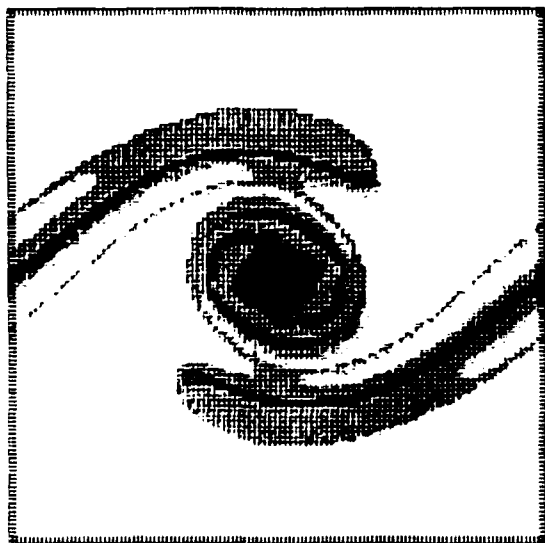
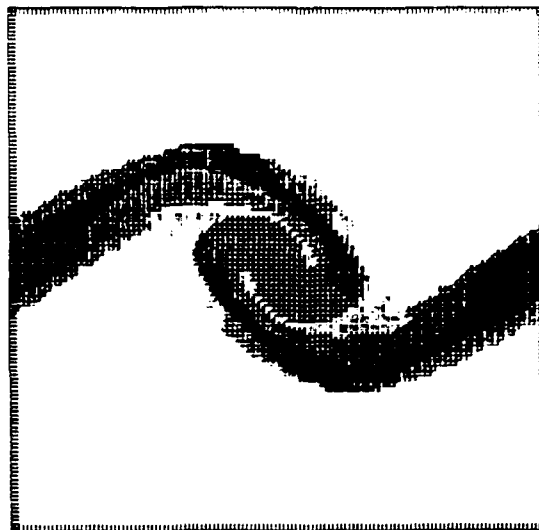
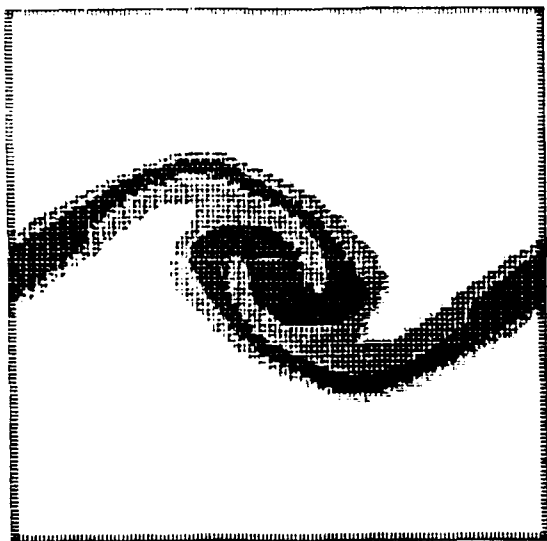
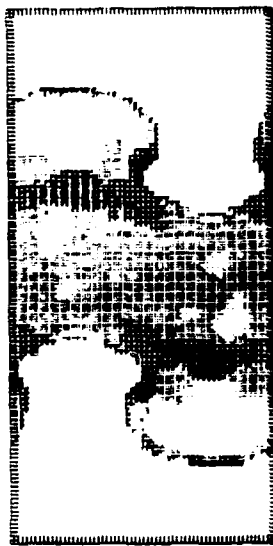
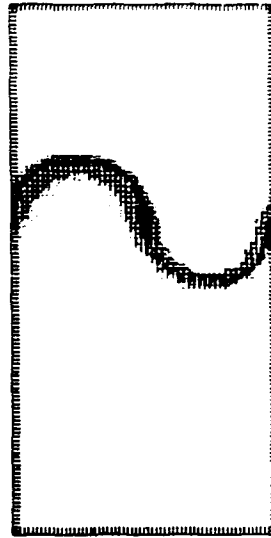
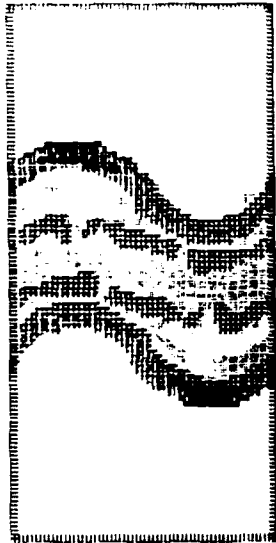


Figure 16a

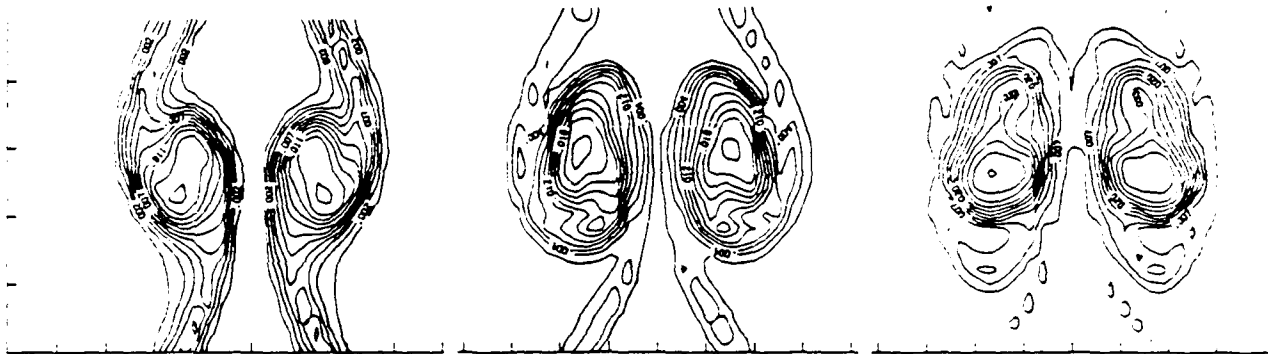


(b)

(c)

Figure 16b, c

(a)



(b)

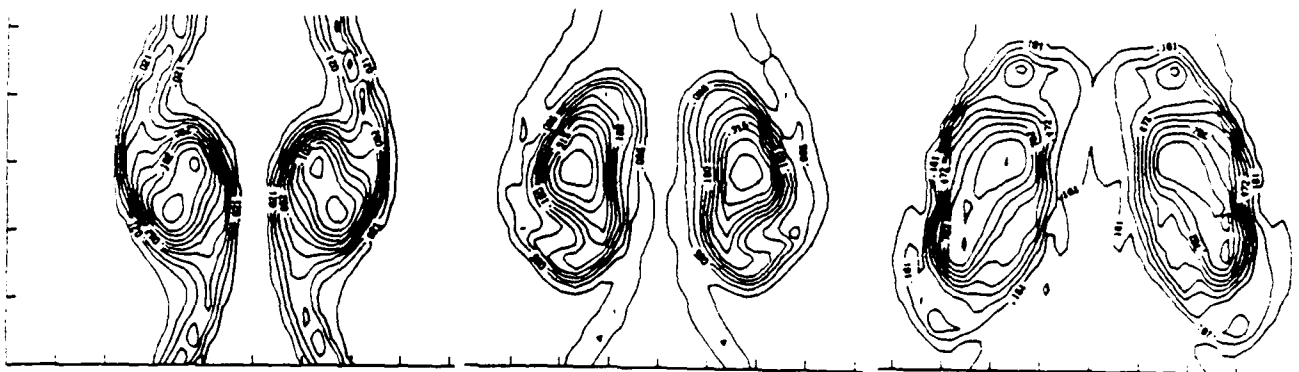
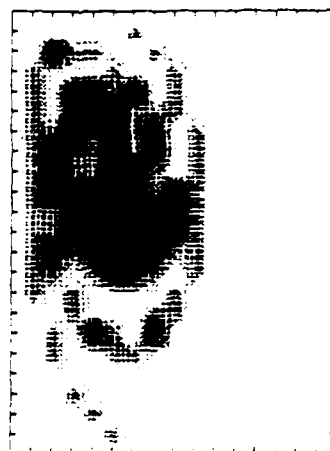
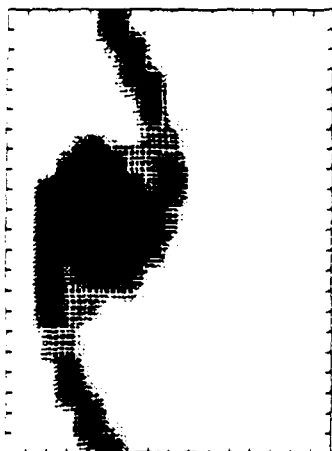


Figure 17

(a)



(b)

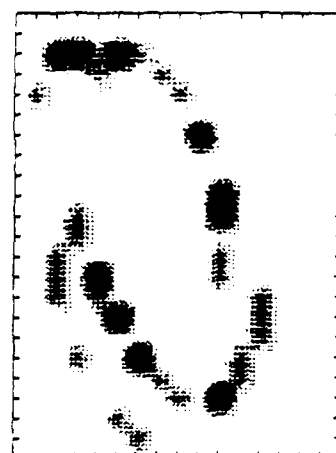
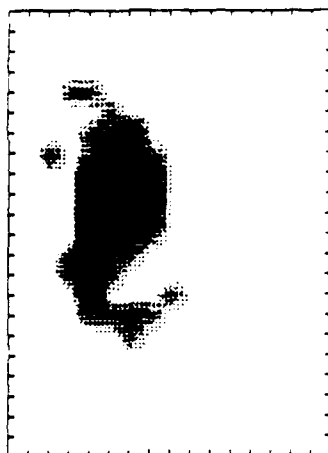
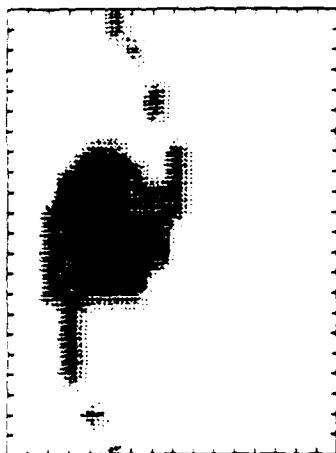
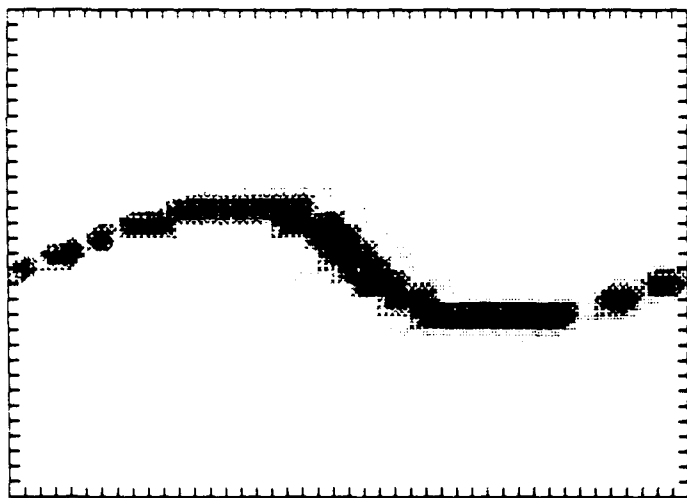
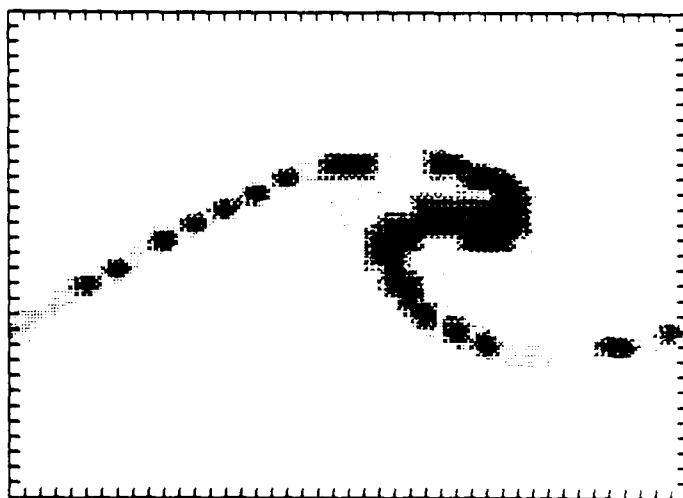


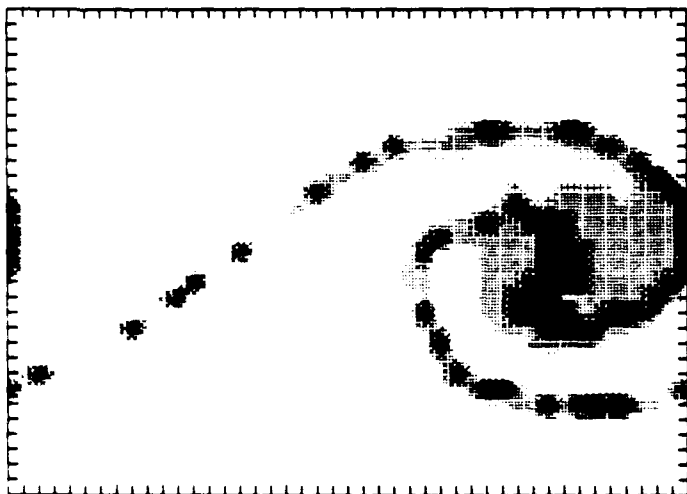
Figure 18



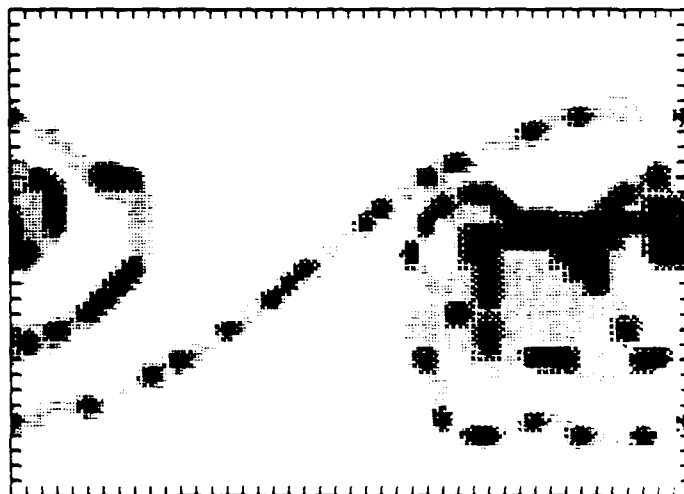
$t = 5.5$



$t = 11.0$

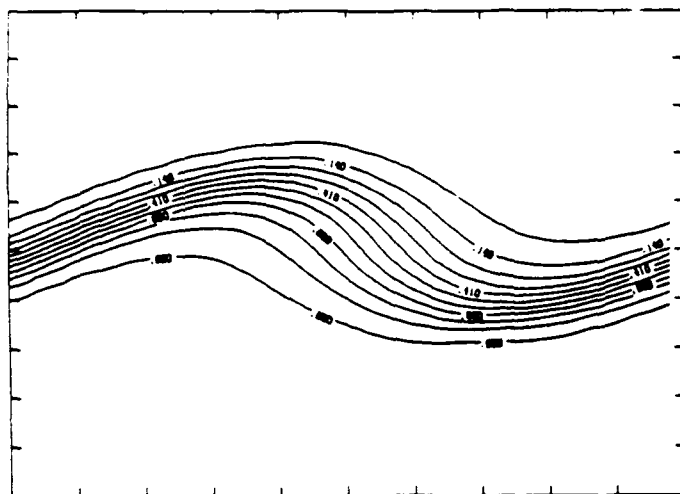


$t = 16.5$

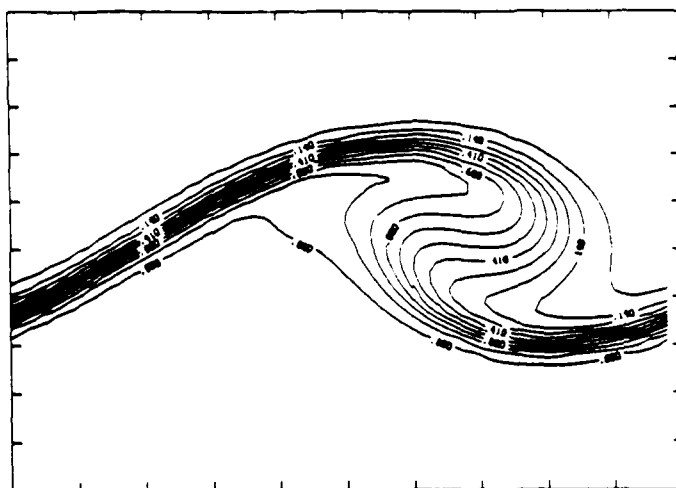


$t = 22.0$

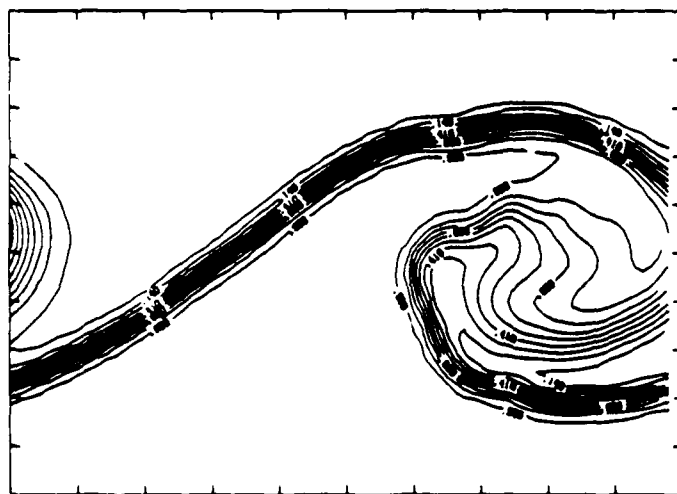
Figure 19a



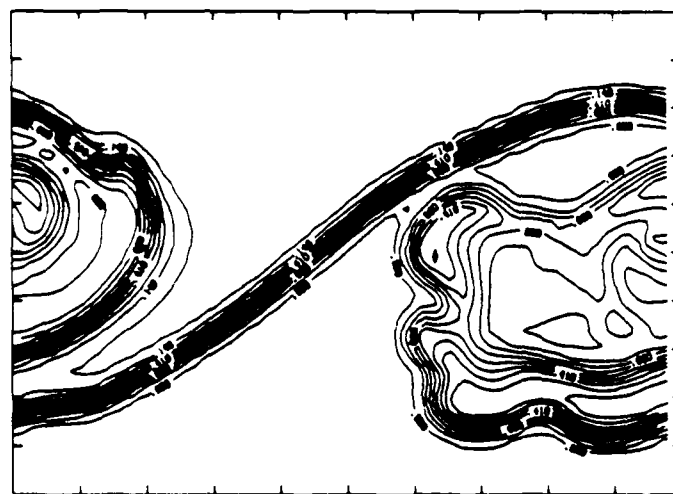
$t = 5.5$



$t = 11.0$



$t = 16.5$



$t = 22.0$

Figure 19b

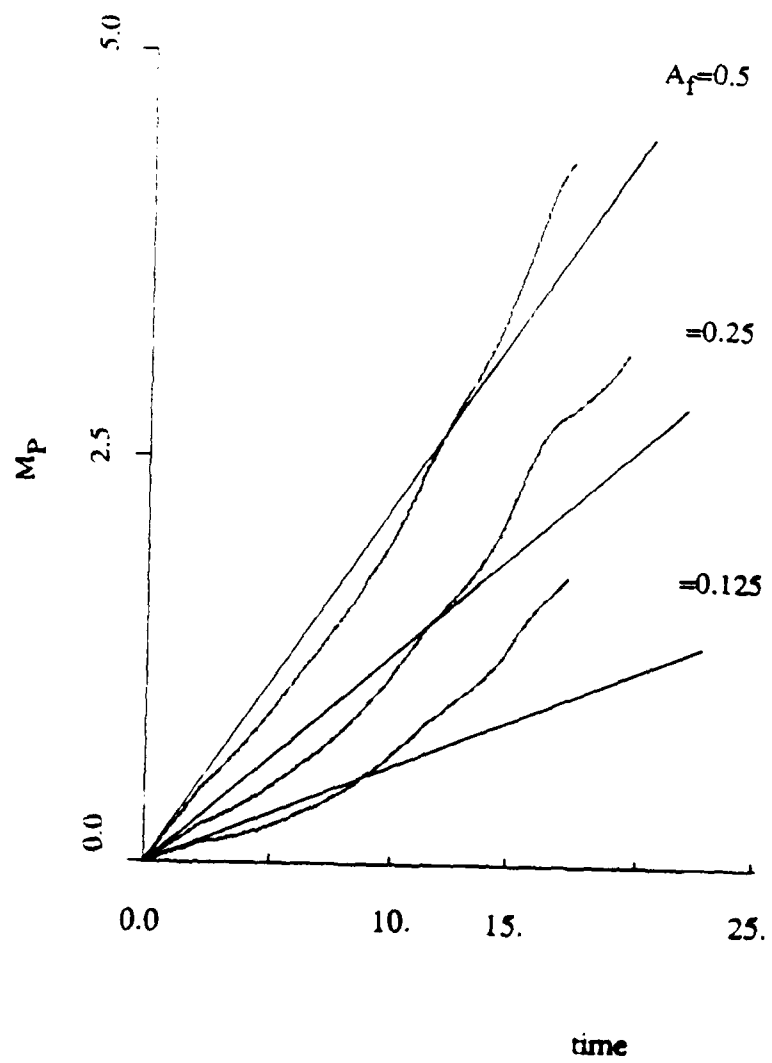


Figure 20

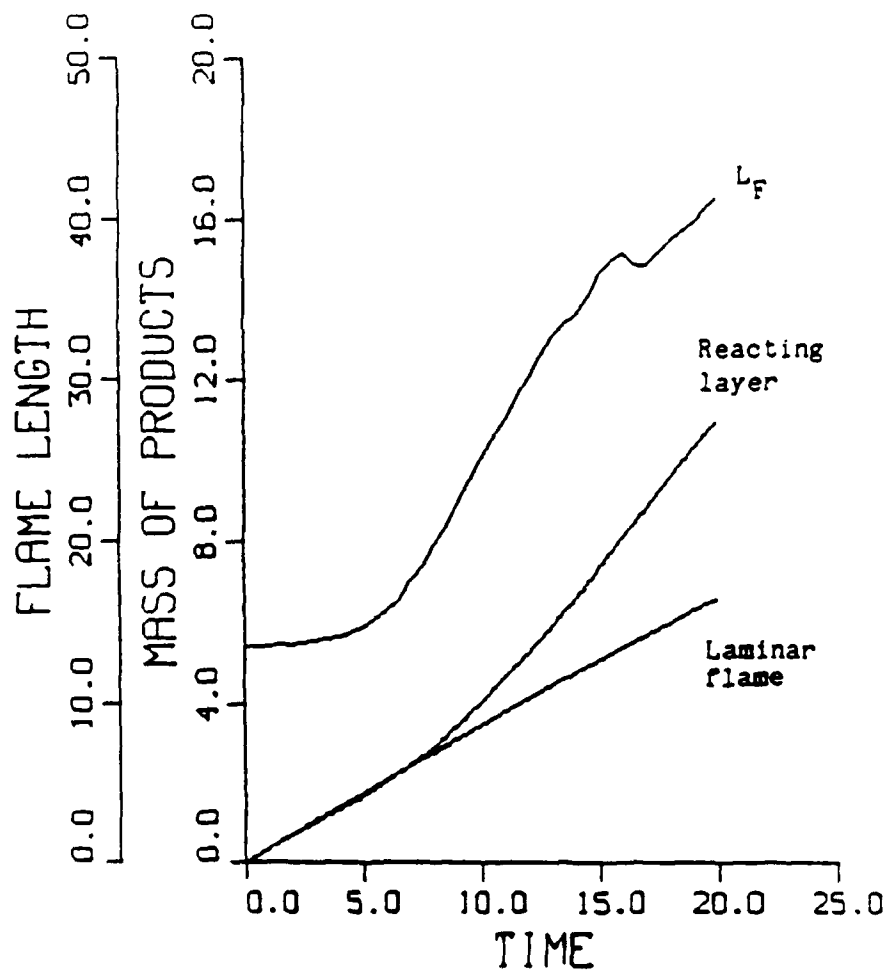


Figure 21